

## Chapter 3

# Comprehensive Evaluation of Novel Compound Benzothiazole-Triazole: Inducing Cell Cycle Arrest, Apoptosis, and Downregulating Bcl-2 Expression in Triple-Negative Breast Cancer Cells

### 3.1 Introduction

Cancer continues to be a prominent contributor to global mortality, resulting in nearly 10 million fatalities in the year 2020 alone.<sup>166</sup> Female breast cancer is the most prevalent cancer globally, ranking second with 2.3 million cases (11.6%) and causing approximately 670,000 deaths (6.9%). By 2050, the number of new cancer cases is anticipated to surpass 35 million, reflecting a 77% growth from the estimated 20 million cases in 2022.<sup>167</sup> Despite significant progress in cancer treatment, the diverse nature of the disease presents considerable obstacles, especially when dealing with aggressive subtypes like triple-negative breast cancer (TNBC). Approximately 10-20% of breast cancers are TNBC, known for the absence of estrogen, progesterone, and HER2 receptors, and have a challenging prognosis and limited therapy choices.<sup>168,169</sup>

Due to the limited availability of specific therapies for TNBC, it is crucial to promptly discover fresh therapeutic targets and create innovative approaches for treatment. A prospective target worth considering is the B-cell lymphoma 2 (Bcl-2) protein, which holds significant importance in regulating apoptosis.<sup>170</sup> The overexpression of Bcl-2 has been correlated with resistance towards chemotherapy and unfavorable clinical results in diverse cancer types, including TNBC.<sup>171</sup> Bcl-2 inhibition can trigger cancer cell apoptosis, which makes it a promising target for anticancer therapy.<sup>172</sup>

Benzothiazole stands out as a notable heterocyclic compound due to its extensive pharmacological properties, notably its potent anticancer effects.<sup>173,174</sup> Its mode of action involves disrupting essential cellular processes that are vital for the survival of cancer cells, such as neddylation inhibition,<sup>175</sup> tubulin polymerization inhibition,<sup>176</sup> VEGFER-2 and BRAF dual inhibition,<sup>177</sup> CA-IX and CA-XII inhibition,<sup>178</sup> Lymphocyte-specific protein

tyrosine kinase (LCK) inhibition.<sup>179</sup> Correspondingly, the 1,2,4-triazole ring has emerged as a privileged structure in the realm of medicinal chemistry, renowned for its exceptional adaptability and effectiveness in the treatment of various diseases, including cancer.<sup>180</sup> Incorporating triazole moieties into drug design has been shown to enhance anticancer activity through various mechanisms, such as inhibition of EGFR,<sup>181</sup> human adenosine A2B protein,<sup>182</sup> CK1 $\gamma$  kinase,<sup>183</sup> EGFR/PARP-1 inhibition<sup>184</sup> and COX-2.<sup>185</sup>

In this study, we aimed to leverage the synergistic potential of benzothiazole and 1,2,4-triazole by integrating these two moieties into a single molecular framework. The rational design included synthesizing benzothiazole-tethered 1,2,4-triazole moieties with an acetamide chain (**Fig. 1**), aiming to improve anticancer therapeutics by combining pharmacophoric elements.<sup>186-191</sup>

Characterization of the synthesized compounds involved the use of <sup>1</sup>H NMR, <sup>13</sup>C NMR, mass spectrometry, and IR spectroscopy to verify their structural integrity and purity. The compounds were subsequently assessed for their anticancer activity against a panel of 60 diverse cancer cell lines through the National Cancer Institute's Developmental Therapeutics Program (NCI DTP-60). The preliminary screening results demonstrated targeted activity against the MDA-MB-231 cell line, which serves as a model for TNBC. The IC<sub>50</sub> value of 14.82  $\mu$ g/mL in MTT assays was observed for the most potent compound. The compound was found to induce G2/M phase arrest and promote early-stage apoptosis, as revealed by mechanistic studies involving cell cycle analysis and apoptosis assays. Furthermore, the Bcl-2 expression assays substantiated the notable suppression of the anti-apoptotic Bcl-2 protein, emphasizing the potential mode of action of the compound. Molecular docking studies were conducted to gain insight into the mechanism of action. These studies revealed that the compounds have strong binding affinities with the key protein Bcl-2 (PDB Id: 4LVT). Molecular dynamics (MD) simulation was used to evaluate the stability and interactions of the compounds in the active site of the target proteins over a period. The computational studies aligned with the experimental findings, demonstrating that the compounds have a strong inhibitory effect on the Bcl-2 protein.

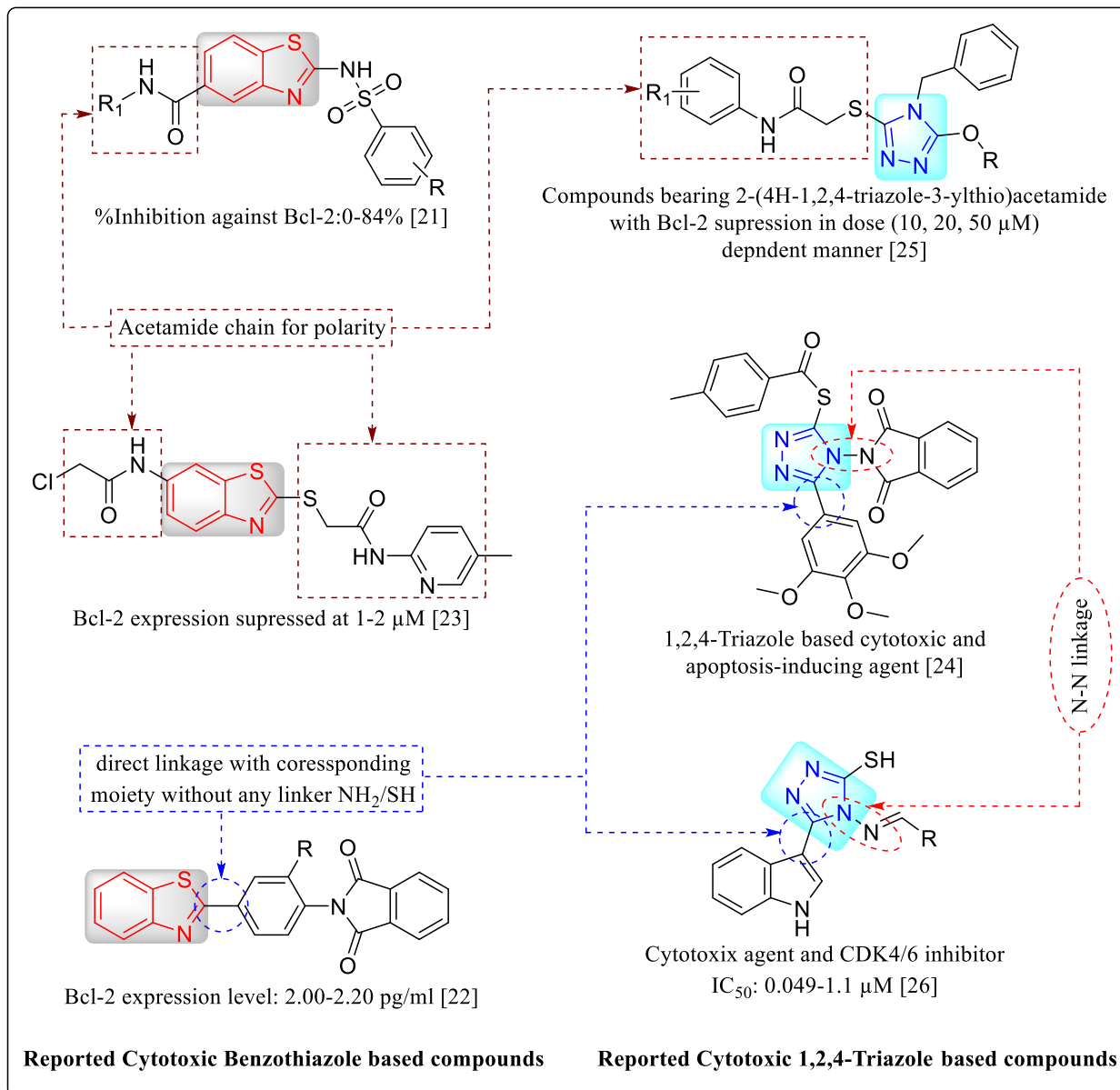


**Figure 1:** Design of novel Benzothiazole tethered 1,2,4-triazole bearing acetamide chain derivative as Bcl-2 inhibitor

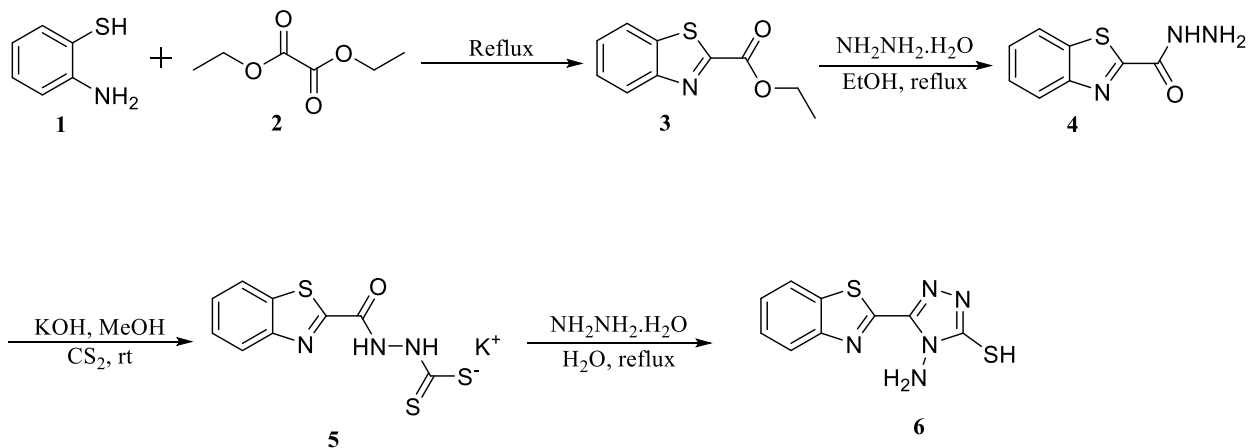
## 3.2 results and discussion

### 3.2.1 Chemistry

The synthesis of the target compounds began with the formation of benzothiazole-2-carboxylate **3** through the reflux reaction of 2-aminothiophenol **1** with diethyl oxalate **2** at 140°C for 4 hours. The reaction proceeded seamlessly, resulting in an excellent yield of the desired product. The subsequent transformation of benzothiazole-2-carboxylate **3** into benzothiazole-2-hydrazide **4** was achieved by reacting it with hydrazine hydrate (99%) in ethanol under reflux conditions. The obtained hydrazide **4** was then converted to dithiocarbazinate salt **5** by treating it with methanolic potassium hydroxide, followed by the addition of carbon disulfide at room temperature. The efficiency of these intermediate reactions sets the stage for the crucial formation of the benzothiazole tethered triazole moiety **6**.

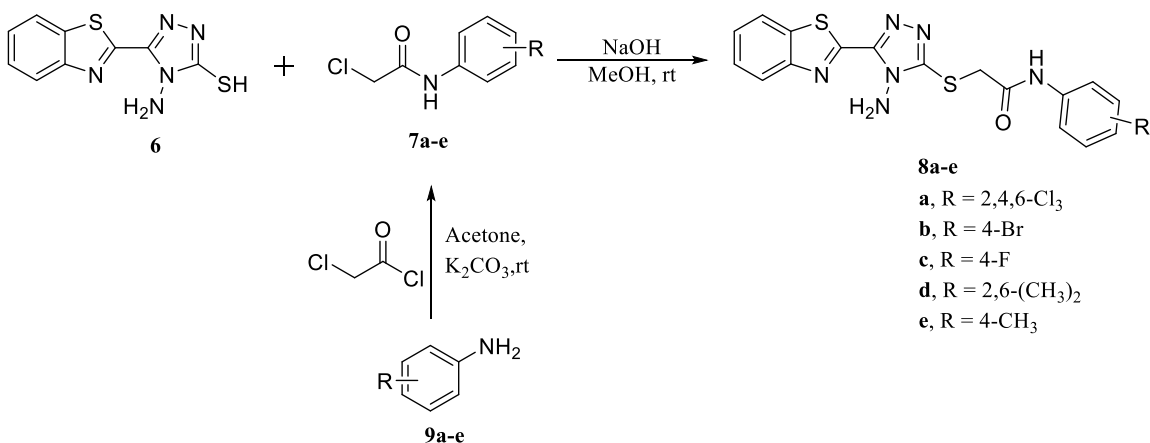
The benzothiazole tethered triazole moiety **6** was synthesized according to the procedure outlined in **Scheme 1**, which involved the reaction of dithiocarbazinate salt **5** with hydrazine hydrate (99%) in an aqueous solution. The structure of compound **6** was confirmed by detailed spectroscopic analysis. The <sup>1</sup>H NMR spectrum of compound **6** showed characteristic signals at  $\delta$  7.61-8.29 ppm, corresponding to the aromatic protons of the benzothiazole ring. The triazole ring's NH<sub>2</sub> protons appeared as singlets around  $\delta$  6.19 ppm. A singlet peak was observed for the thiol proton, with a chemical shift at downfield  $\delta$  14.38 ppm. The <sup>13</sup>C NMR spectrum further supported the formation of compound **6**, with a distinct peak at  $\delta$  167.36 ppm corresponding to the C-SH group, and peaks at  $\delta$  144.94 and 152.55 ppm, indicating the C-C bond linkage between triazole and benzothiazole ring.





**Scheme 1:** Synthesis pathway illustrating the formation of the key intermediate benzothiazole-triazole compound starting from 2-aminothiophenol

The synthesis of 2-chloro-N-phenylacetamide derivatives **7a-e** was conducted using a previously established method with slight adjustments.<sup>192</sup> The method involved the combination of various aniline derivatives **9a-e** with chloroacetyl chloride in the presence of potassium carbonate in acetone, resulting in the production of derivatives **7a-e** as illustrated in **Scheme 2**. The final step involved the nucleophilic substitution of benzothiazole tethered triazole **6** with 2-chloro-N-phenylacetamide derivatives **7a-e** in the presence of sodium hydroxide in methanol at room temperature. The reaction resulted in the formation of the final target compounds, 2-((4-amino-5-(benzo[d]thiazol-2-yl)-4H-1,2,4-triazol-3-yl)thio)-N-phenylacetamide derivatives **8a-e**, with high yields.



**Scheme 2:** Detailed synthetic route to the final Benzothiazole-triazole bearing N-phenylacetamide derivatives **8a-e**

The structures of the final compounds **8a-e** were validated using comprehensive spectroscopic analyses. The  $^1\text{H}$  NMR spectra of compounds **8a-e** demonstrated characteristic signals indicative of the presence of aromatic protons. Aromatic ring protons from the benzothiazole moiety and the phenylacetamide moiety were identified at  $\delta$  8.28-7.05 ppm. The protons of  $\text{NH}_2$  from the triazole were detected as singlets, with chemical shifts ranging from  $\delta$  6.57 to 6.56 ppm. The successful attachment of the N-phenylacetamide chain to the thiol group was confirmed by the presence of characteristic peaks in the  $^1\text{H}$  NMR spectrum. These peaks, observed at  $\delta$  4.33 to 4.24 ppm, were attributed to the methylene protons. The structural assignments were further supported by the  $^{13}\text{C}$  NMR spectra, which showed clear chemical shifts for the carbonyl carbon ( $\delta$  ~165-167 ppm) and the carbon connected to the thiol group ( $\delta$  ~154 ppm). The benzothiazole and triazole moieties are connected by a C-C linkage, which establishes the stability of the carbon framework. The benzothiazole-associated carbon exhibits chemical shifts between  $\delta$  154.70-155.60 ppm, while the triazole-associated carbon shows shift between  $\delta$  148.62-149.19 ppm. The IR spectra displayed distinct absorption bands at 3248-3271  $\text{cm}^{-1}$ , indicative of the triazole's  $\text{NH}_2$  stretching vibrations, and at 3039-3178  $\text{cm}^{-1}$ , suggesting the N-H stretching in the acetamide group. The C=O stretching of the acetamide group was confirmed by a band around 1651-1689  $\text{cm}^{-1}$ . Analysis of the final compounds using mass spectrometry confirmed the molecular weights, which were consistent with the proposed structures.

### 3.2.2 Single-Dose Cytotoxicity Screening

The cytotoxic potential of the synthesized benzothiazole tethered triazole derivatives **8a-e** was assessed by the National Cancer Institute's Developmental Therapeutics Program (DTP-60). The compounds were screened at a fixed concentration of 10  $\mu\text{M}$  against a diverse panel of approximately sixty different human cancer cell lines. The cell lines were derived from nine different cancer types, such as leukemia, lung cancer, colon cancer, CNS cancer, melanoma, ovarian cancer, renal cancer, prostate cancer, and breast cancer. Growth inhibition was quantified as a growth percentage (GP) relative to untreated controls

(Figure 2-6). The mean growth percentage is a crucial factor that shows the average growth response of all the cell lines in the panel to the compound (Table 1). The range of growth percentage helps to elucidate the variability in the compound's activity, showcasing the full range between the lowest and highest growth percentages observed. Moreover, the evaluation of a compound's therapeutic potential relies on the concepts of cytostatic and cytotoxic effects. The cytostatic effect is the ability of a compound to stop cell growth without causing cell death. It was measured by the percentage of cell lines that showed a growth rate between 0% and 50%. Conversely, the cytotoxic effect was measured by the percentage of cell lines that displayed a negative growth rate, indicating cell death.

**Table 1:** Comparative Anticancer Screening of Compounds 8a-e at 10  $\mu$ M

Compounds	Single dose data at 10 $\mu$ M concentration				
	Mean growth (%)	Range of growth (%)	Positive cytostatic effect	Positive cytotoxic effect	Sensitive cell lines
8a	54.27	-13.97 to 108.74	22/54	2/54	OVCAR-4, HS 578T
8b	74.11	7.70 to 142.26	6/54	0/54	MDA-MB-231
8c	76.78	-15.12 to 161.04	6/54	1/54	MDA-MB-231, HCT-116
8d	94.46	75.83 to 106.88	0/54	0/54	UACC-62, MDA-MB-468
8e	98.83	4.70 to 140.80	1/59	0/59	MDA-MB-231, SF-539

Compound **8a** demonstrated strong cytotoxic activity, reducing MDA-MB-231 cell growth to just 12.67% of the control (Figure 2). The cytotoxicity of this derivative was also observed against OVCAR-4 (-13.97%) and HS 578T (-4.40%), indicating its potential

efficacy against multiple cancer types. In addition, **8a** displayed promising activity against a NSCL cancer, particularly NCI-H226 (11.37%), and showed effectiveness against CNS cancer, specifically SNB-19 (13.98%). Compound **8b** effectively suppressed the growth of MDA-MB-231 cells by 7.70%, and also displayed strong activity against the HCT-116 colon cancer cell line, inhibiting growth by 13.57% (**Figure 3**). Additionally, this compound exhibited significant effectiveness against CNS cancer, specifically against the SF-539 cell line, resulting in a growth percentage of 24.89%. The MDA-MB-231 cell line was highly susceptible to derivative **8c**, showing a growth percentage of -15.12%. Moreover, **8c** demonstrated significant suppression of colon cancer in the HCT-116 cell line, exhibiting a growth rate of only 2.84%. It also exhibited remarkable efficacy against CNS cancers, particularly in the SF-539 and U251 cell lines, with growth rates of 2.92% and 9.42% respectively (**Figure 4**). The cytotoxic activity of derivative **8d** was observed in breast cancer cell lines. It reduced the growth of the MDA-MB-231 cell line to 88.93% and demonstrated significant inhibition of the MDA-MB-468 cell line, with a growth percentage of 80.26% (**Figure 5**). The cytotoxic activity of Compound **8e** against the MDA-MB-231 cell line was potent, leading to a substantial growth inhibition of 4.70%. However, the compound exhibited only moderate activity in the remaining tested cell lines (**Figure 6**). The single dose screening data showed that all synthesized benzothiazole tethered triazole derivatives **8a-e** had a consistent and significant cytotoxic effect on the MDA-MB-231 cell line. This cell line is a representative model of triple-negative breast cancer (TNBC). The uniform activity observed in the series emphasizes the promise of these compounds as targeted therapeutics for TNBC, justifying the selection of MDA-MB-231 for detailed biological analysis.

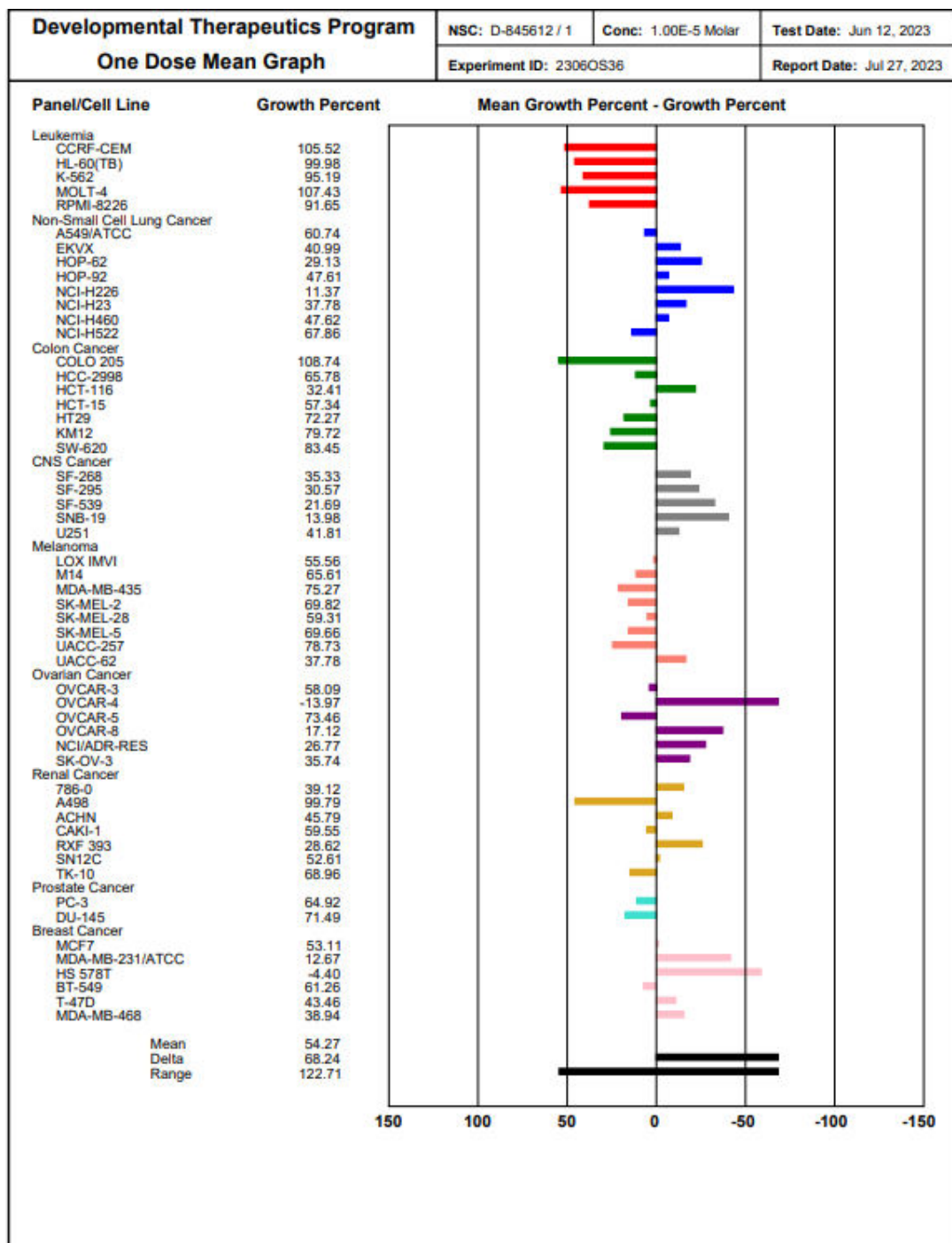


**Figure 2:** One-dose cytotoxicity analysis of Compound 8a on various cancer cell lines. Mean growth percentages reflect the compound's activity across a range of tumor types

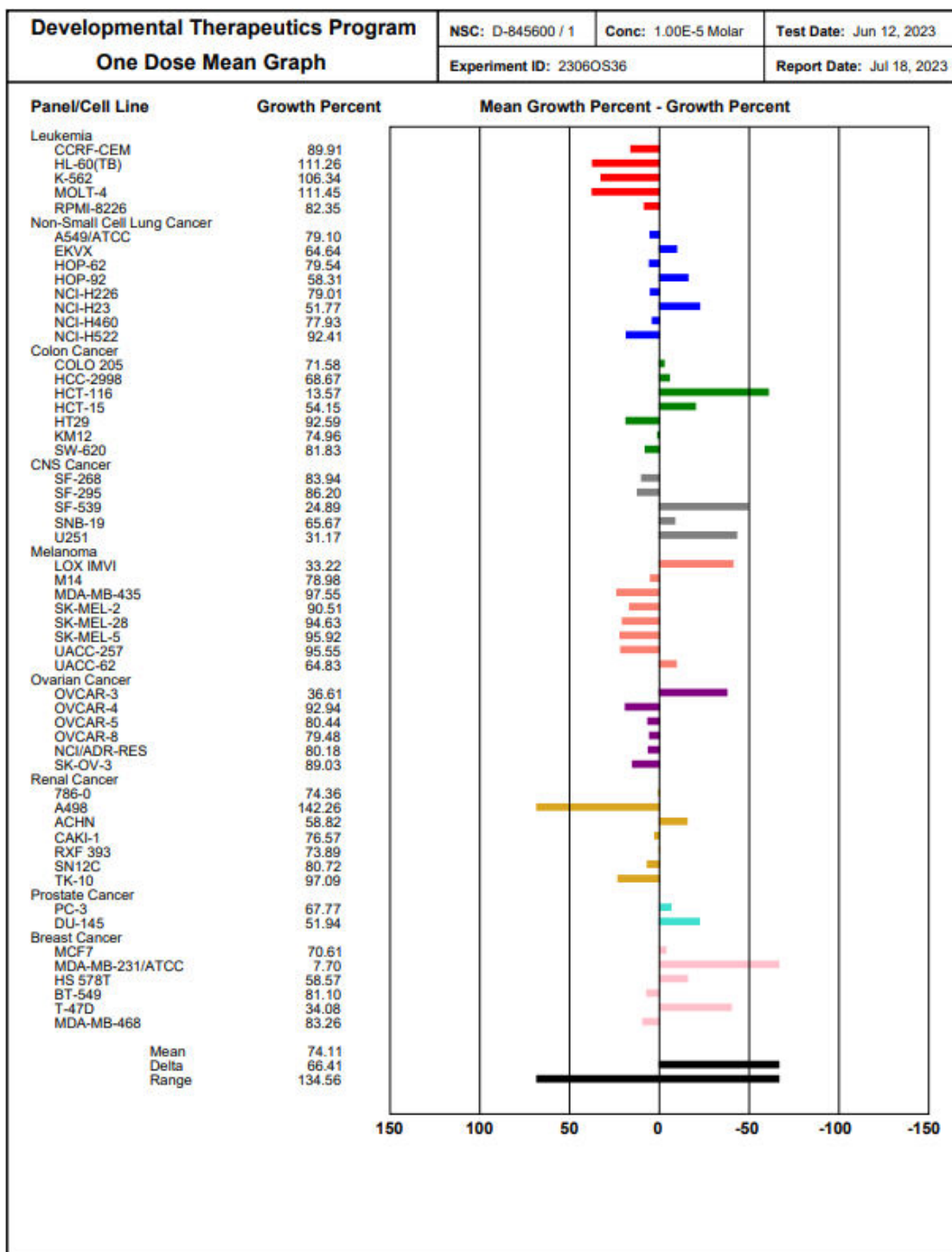


**Figure 3:** Evaluation of Compound 8b's cytotoxic activity via one-dose assay on a panel of cancer cell lines. Bar graph illustrates differential sensitivity.

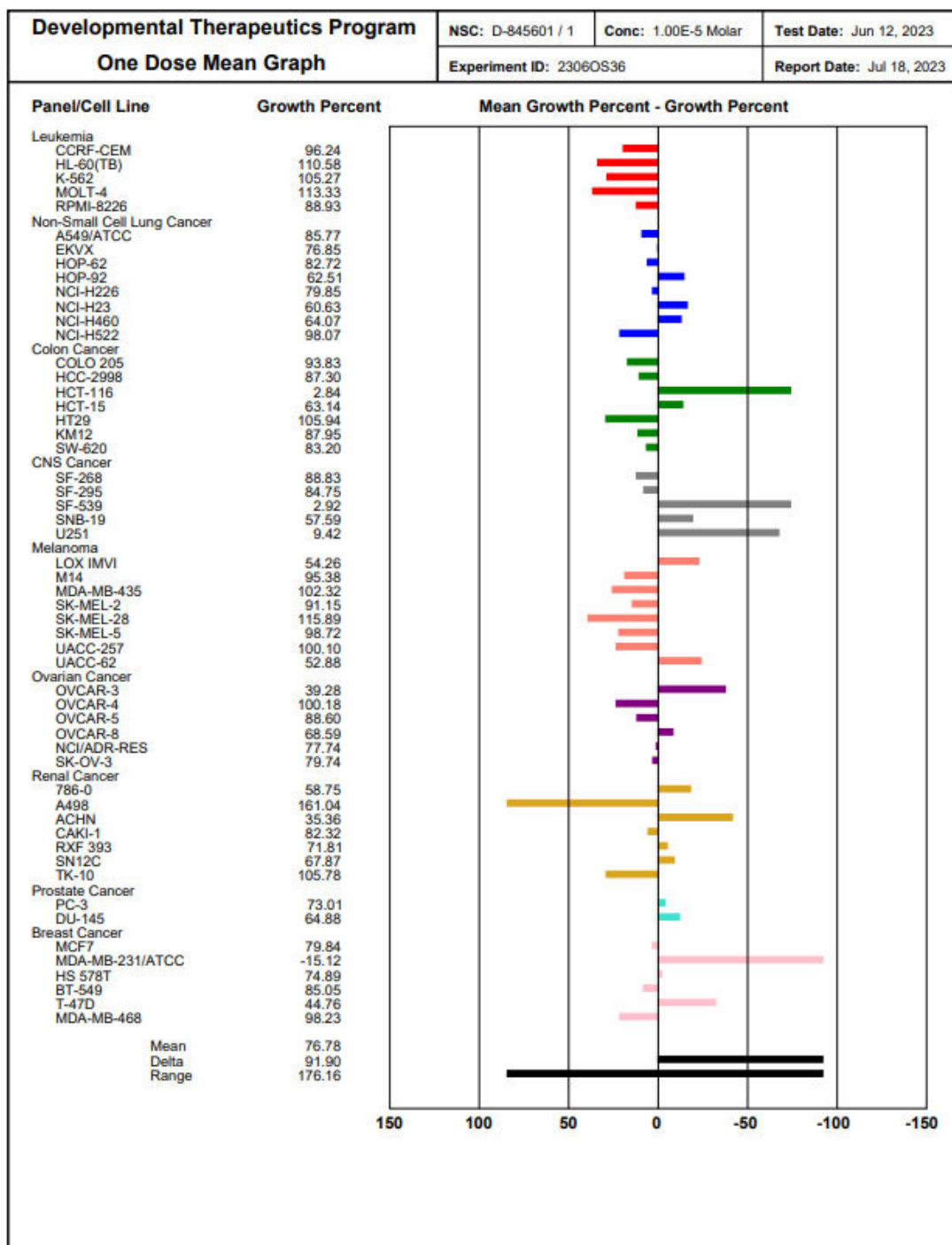


**Figure 4:** Compound 8c one-dose assay cytotoxicity profile across leukemia, lung, colon, CNS, melanoma, ovarian, renal, prostate and breast cancer cell lines

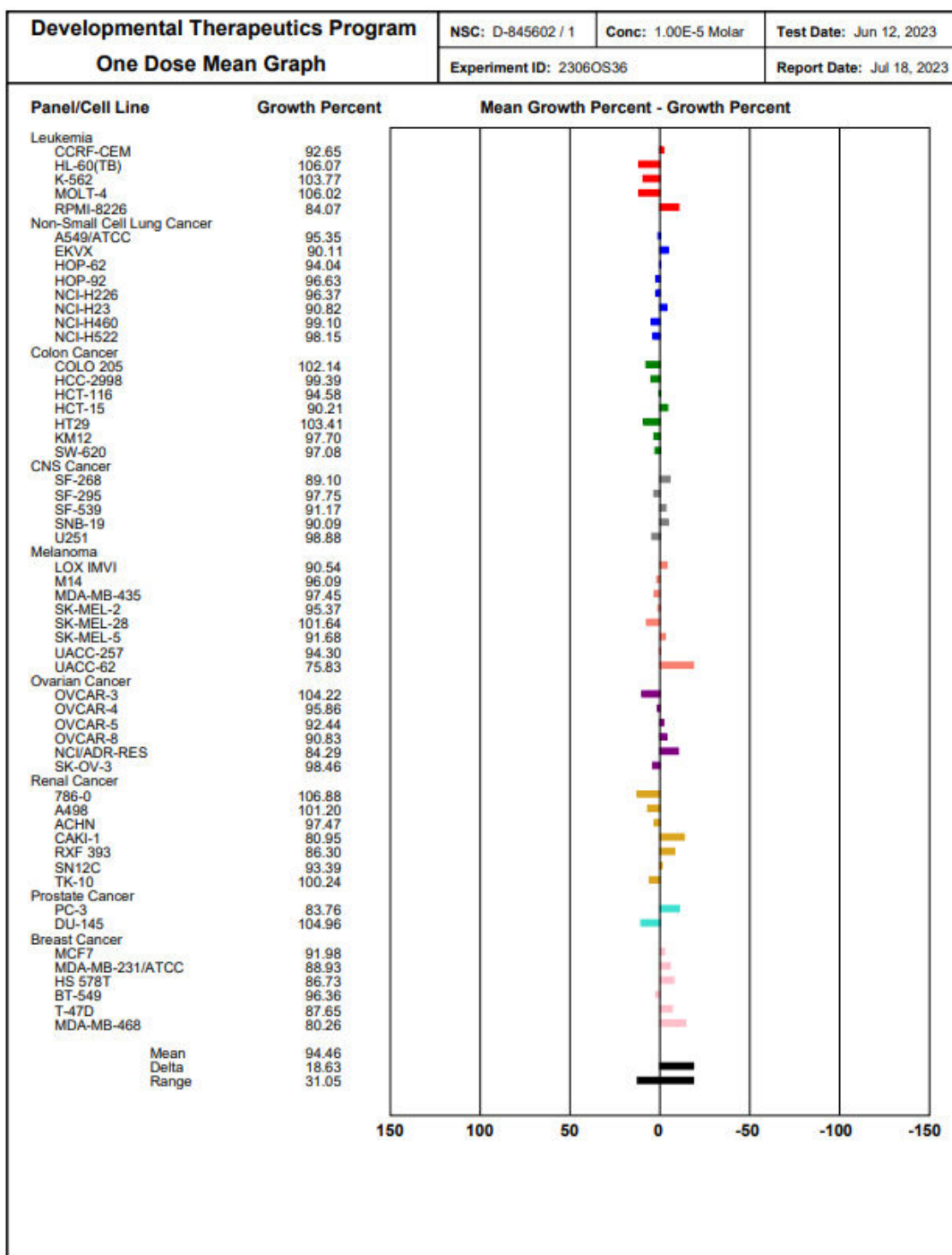


**Figure 5:** Comparative analysis of Compound 8d on MDA-MB-231 and other breast cancer cell lines, highlighting significant growth inhibition observed via the one-dose assay



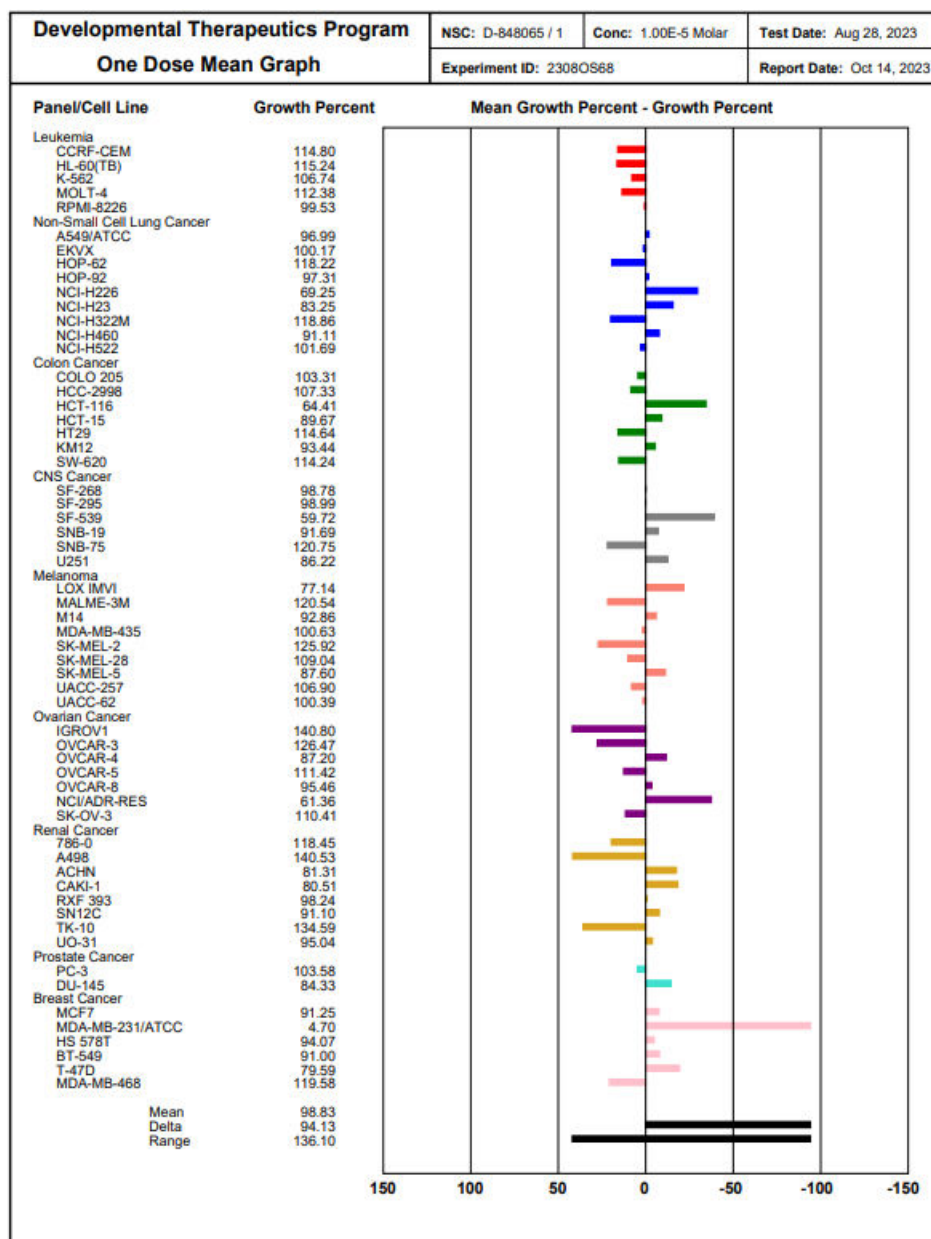


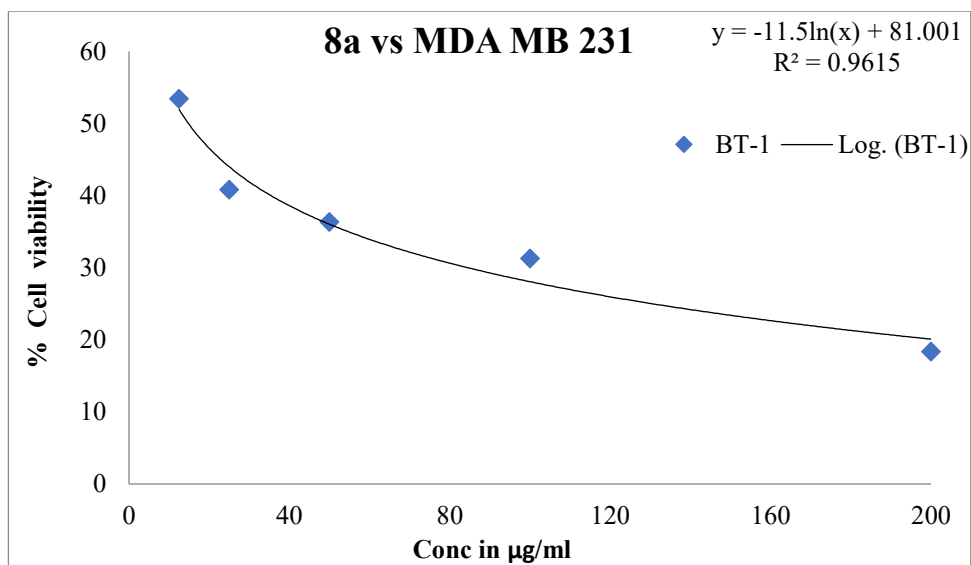
**Figure 6:** One-dose cytotoxicity assay results for Compound 8e against various solid tumors and hematologic cancers, indicating potent activity against MDA-MB-231 at a single concentration

### 3.2.3 *In Vitro* Cytotoxicity Assessment and Dose-Response Analysis

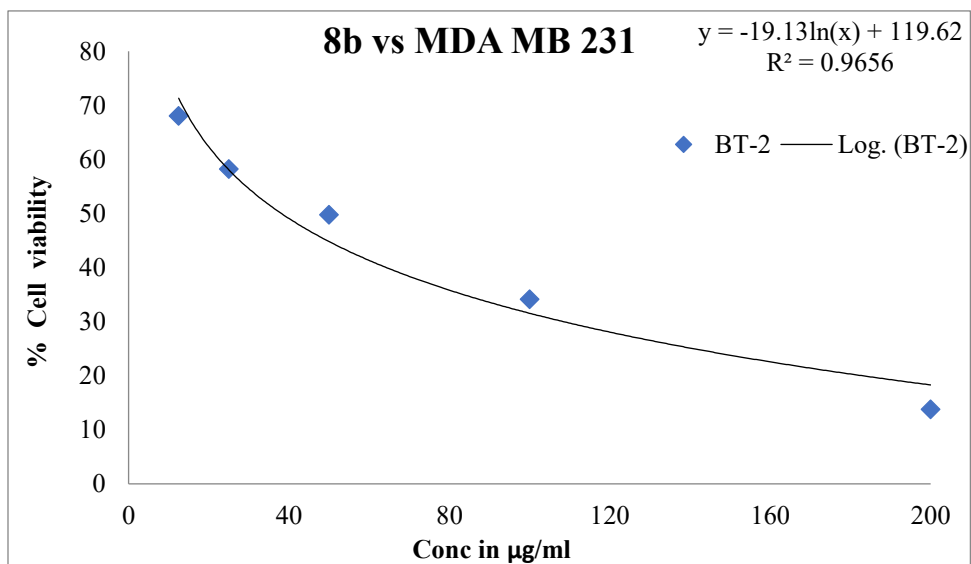
The synthesized benzothiazole tethered triazole derivatives (**8a-e**) were evaluated for their cytotoxic activity against the MDA-MB-231 triple-negative breast cancer (TNBC) cell line using the MTT assay. The results consistently showed a significant dose-dependent

decrease in cell viability for all compounds, suggesting their potent anticancer properties. The % cell viability results, demonstrating a dose-dependent pattern, can be found in **Figure 7**.

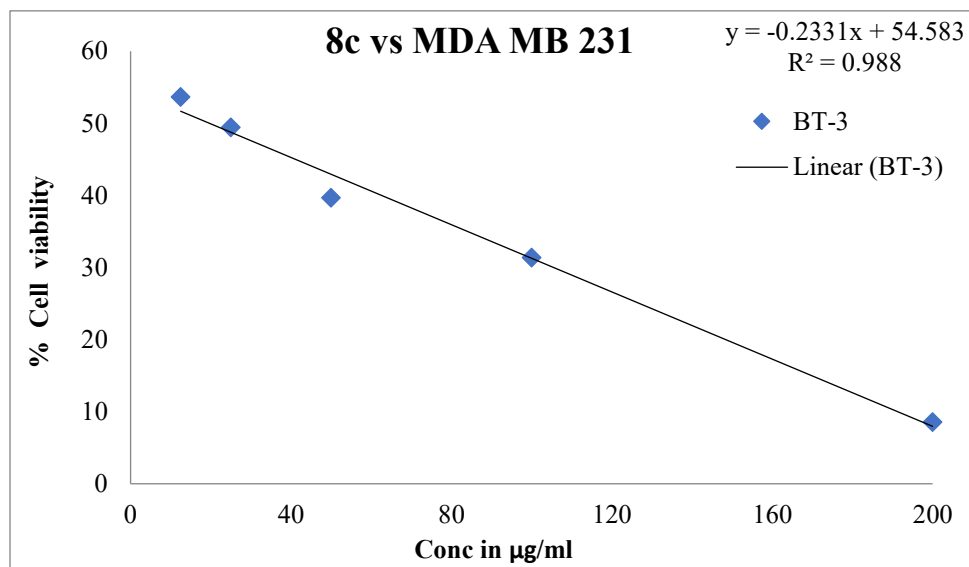
(A)



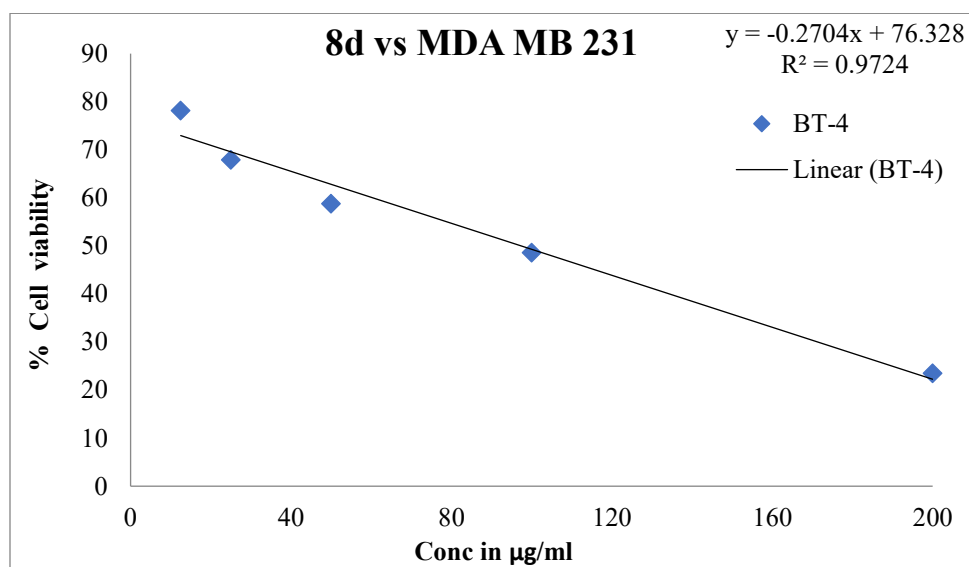
(B)



(C)



(D)



(E)

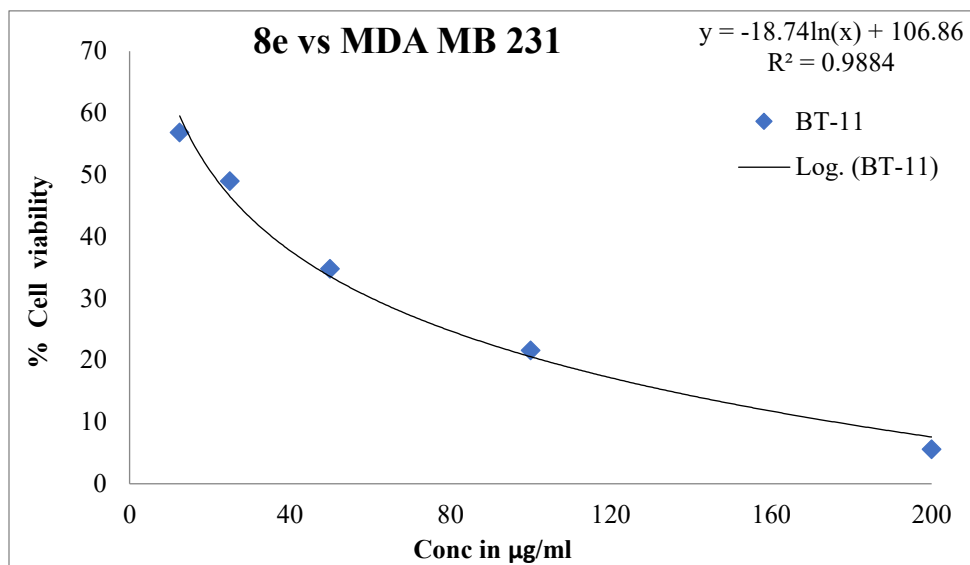


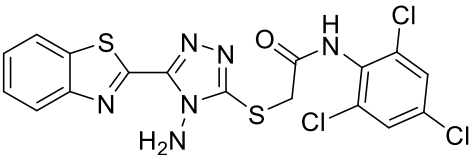
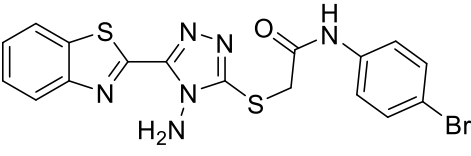
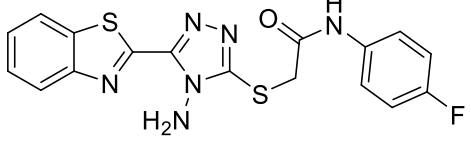
**Figure 7:** (A) Dose-response curve of compound 8a showing the percent cell viability inhibition against MDA-MB-231 cells (B) Dose-response curve of compound 8b showing the percent cell viability inhibition against MDA-MB-231 cells (C) Linear dose-response curve of compound 8c demonstrating the inhibition of cell viability in MDA-MB-231 cells (D) Linear dose-response curve of compound 8d representing the inhibitory effect on MDA-MB-231 cell viability (E) Dose-response curve of compound 8e illustrating the percent inhibition of MDA-MB-231 cell viability

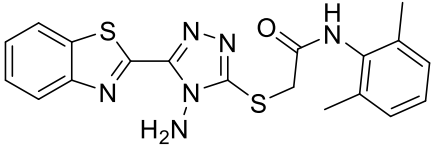
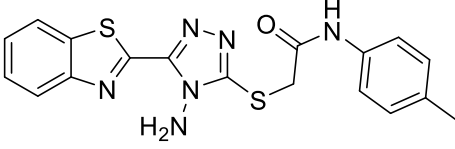
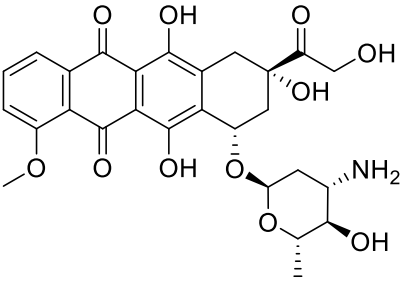
Compound **8e** showed a substantial decrease in cell viability, with the most pronounced effects observed at higher concentrations, where viability dropped by nearly less than half, suggesting a strong potential to inhibit the proliferation of TNBC cells. In comparison to **8e**, derivative **8b** exhibited slightly lower cytotoxic profile, with cell viability being reduced to less than a third at the highest concentration. The compound **8c** exhibited a similar pattern, showing a consistent decrease in cell viability at all concentrations, which emphasizes its effectiveness as a cytotoxic agent. Notably, **8a** emerged as the most potent compound in this series, with an exceptional reduction in cell viability, particularly at the highest concentrations where the viability was almost entirely abrogated. This remarkable cytotoxicity underscores the derivative **8a** potential as a leading candidate for further mechanistic studies. Despite being slightly less potent than **8a**, molecule **8d** showed

significant cytotoxicity and a notable decrease in cell viability, further confirming the effectiveness of the series.

The cytotoxic potential of these compounds was quantitatively assessed through determination of their  $IC_{50}$  values using the MTT assay, validating their effectiveness. The  $IC_{50}$  values, which offer valuable insights into the inhibitory concentrations of the compounds, are consolidated in **Table 2**. Based on the collective findings of the MTT assay, it can be concluded that the benzothiazole tethered triazole derivatives have significant anticancer activities against TNBC, with particular emphasis on the promising potential of **8d**. The dose-response characteristics exhibited by these compounds, along with their consistent efficacy at different concentrations, highlight their potential as targeted therapy for TNBC. The therapeutic potential of these compounds has been further explained through mechanistic studies, which have provided a more comprehensive understanding of their modes of action.

**Table 2:**  $IC_{50}$  Values Determined by MTT Assay in MDA-MB-231 Cells

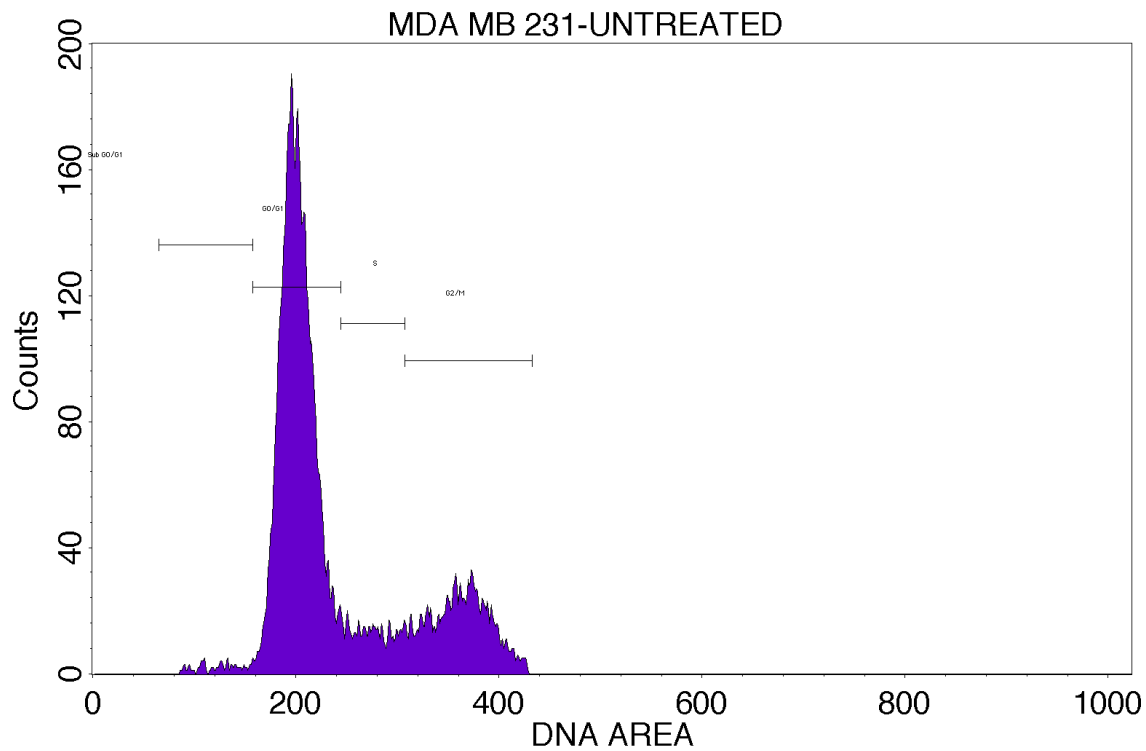
Compounds	$IC_{50}$ values
 <p style="text-align: center;"><b>8a</b></p>	14.82 $\mu\text{g/mL}$
 <p style="text-align: center;"><b>8b</b></p>	38.06 $\mu\text{g/mL}$
 <p style="text-align: center;"><b>8c</b></p>	19.66 $\mu\text{g/mL}$

 <b>8d</b>	97.36 $\mu\text{g/mL}$
 <b>8e</b>	20.78 $\mu\text{g/mL}$
 <b>Doxorubicin</b>	1.00 $\mu\text{g/mL}$

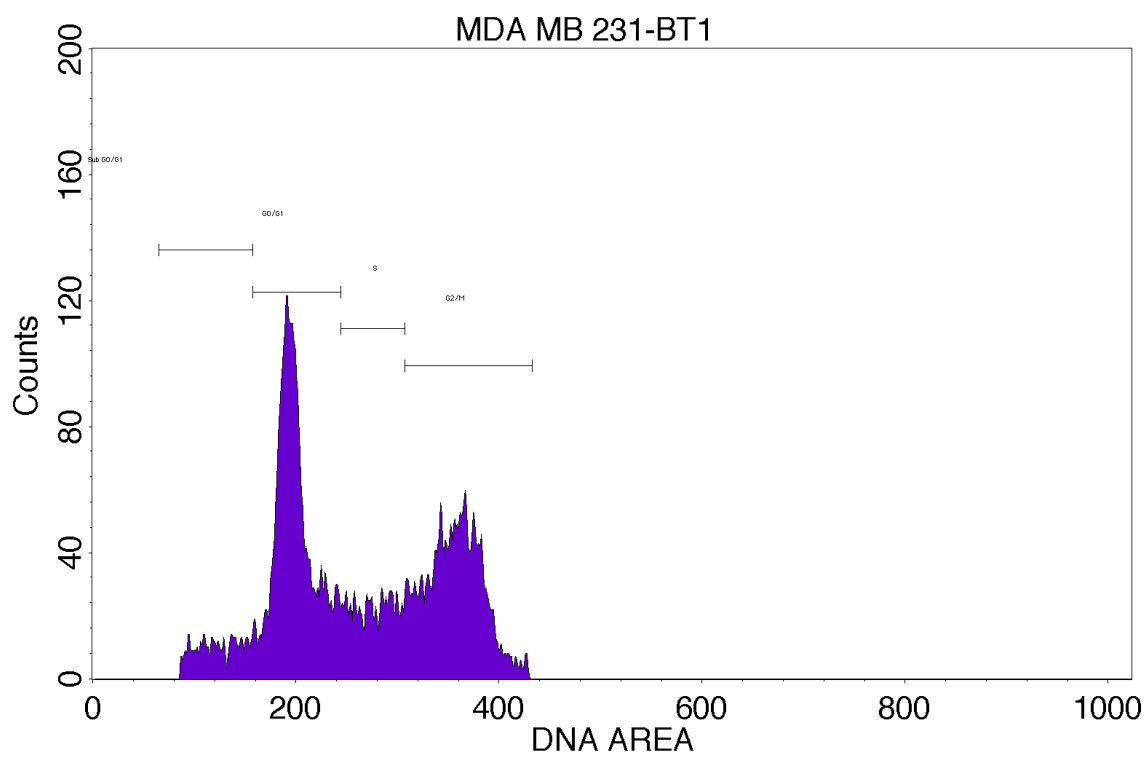
### 3.2.4 Cell Cycle Alterations Induced by Benzothiazole-Tethered Triazole Derivative

The cell cycle distribution in both untreated and compound-treated MDA-MB-231 cells was thoroughly examined using flow cytometry. Propidium iodide (PI) was utilized as a fluorescent dye to stain the nucleic acids. PI is a widely used dye that binds to double-stranded nucleic acids and accurately measures DNA content in cells, enabling the identification of cell cycle phases. The FL3 detector with a 620 nm band-pass filter was used to collect the PI fluorescence, which allowed for precise quantification of the different cell cycle phases. This technique is highly effective for assessing the cell cycle distribution of complete cell populations, particularly when cells are treated with 70% ethanol to ensure adequate permeabilization and dye penetration.

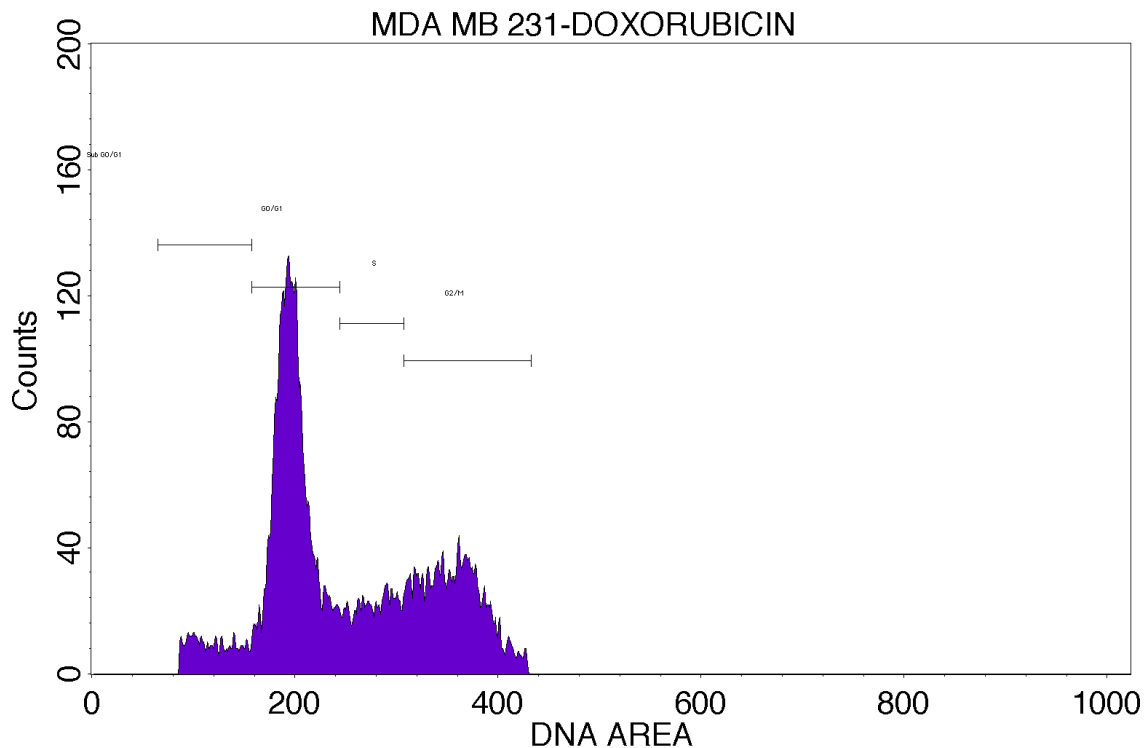
(a)



(b)



(c)



(d)

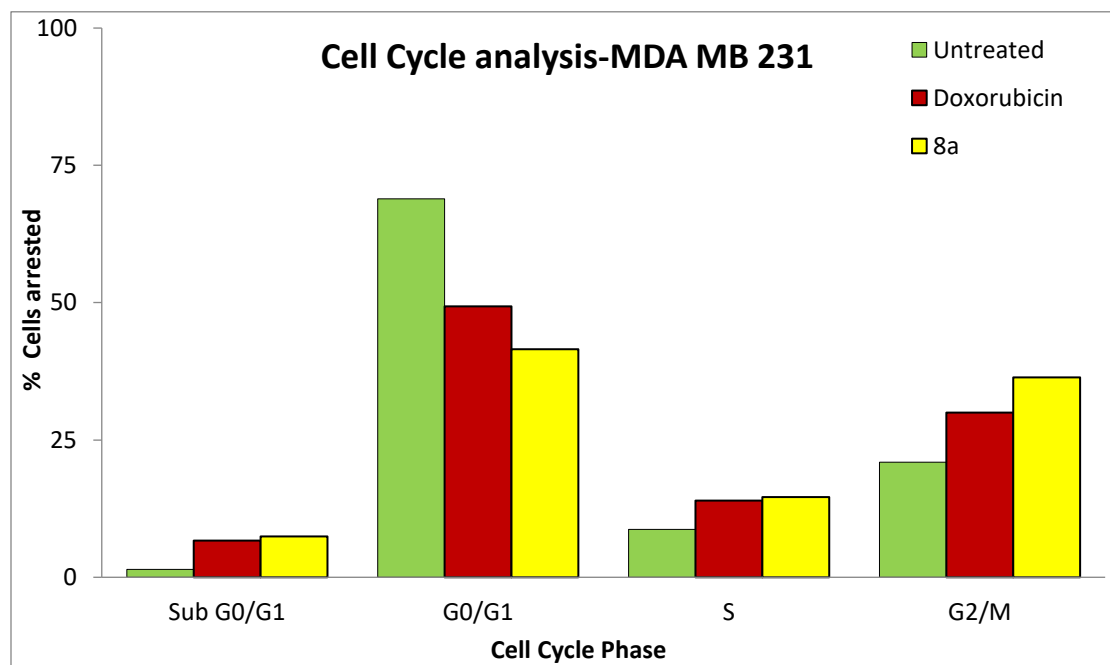




**Figure 8:** (a), (b) and (c) Histogram Illustrating the untreated and Impact of Compound 8a and std. doxorubicin on Cell Cycle Progression in MDA-MB-231 Cells, Indicating Significant G2/M Phase Accumulation (B) Distribution of MDA-MB-231 cells across different phases of the cell cycle following treatment with Compound 8a at IC<sub>50</sub> concentration (14.82 µg/ml) compared to untreated control

The administration of the test compound at its IC<sub>50</sub> concentration led to significant alterations in the cell cycle phases, as outlined in **Figure 8**. A noticeable halt in the G2/M phase was observed, and this was accompanied by a proportional reduction in the population of the G0/G1 phase. In addition, the compound **8a** treated cells exhibited a significant increase in the SubG1 population, signifying DNA damage or apoptosis, as opposed to the untreated control.

The G2/M phase is a crucial stage in the cell cycle, where cells verify the integrity and replication of DNA before entering mitosis.<sup>193</sup> The observed arrest during this phase is likely due to the compound causing DNA damage. This damage activates pathways that respond to DNA damage, leading to the activation of checkpoint proteins such as p53 and the inhibition of cyclin-dependent kinases (CDKs). This inhibition prevents the cell from progressing into mitosis, halting cell division.<sup>194</sup> When cells are arrested at the G2/M phase, several downstream effects can occur. Mitotic catastrophe can occur as a consequence of prolonged arrest, wherein cells attempt to initiate mitosis despite DNA damage, ultimately leading to apoptosis.<sup>195</sup> This finding aligns with the observed increase in the SubG1 population in treated cells. The increase suggests that there is a rise in apoptotic or necrotic cells. The interruption of the G2/M phase effectively halts cell growth, leading to decreased cell viability, as shown by the cytotoxic effects observed in the MTT assay.

### 3.2.5 Induction of Apoptosis in MDA-MB-231 Cells

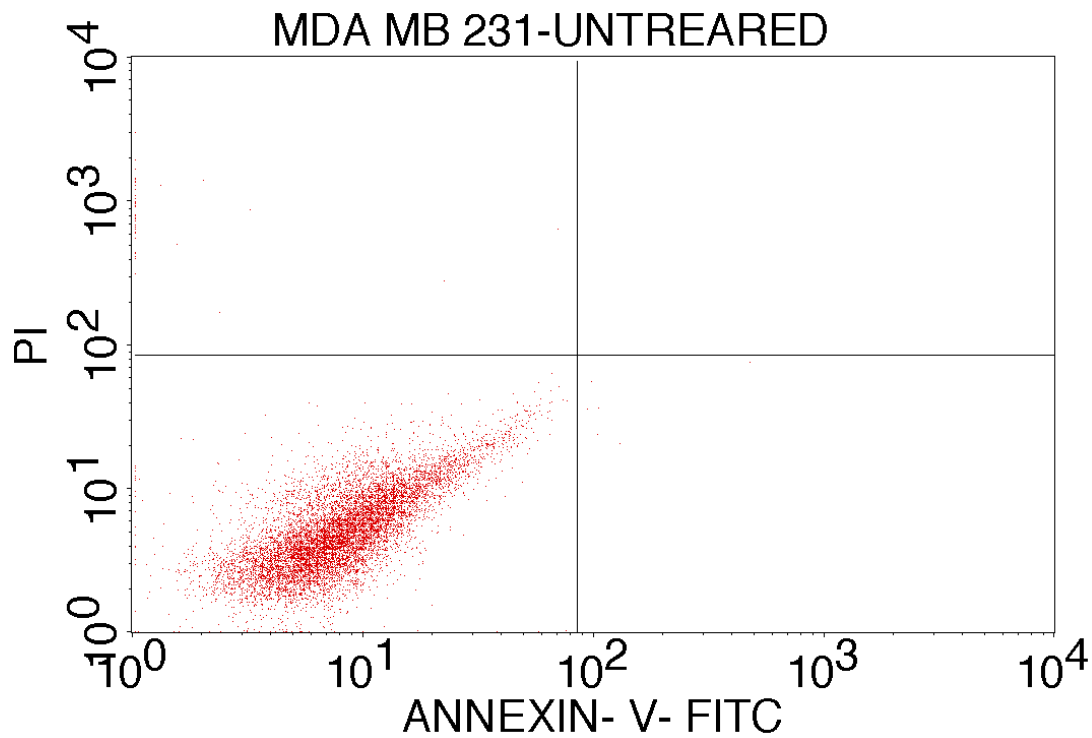
The assessment of apoptosis was executed through the utilization of flow cytometry, employing the Annexin V/Propidium Iodide (PI) staining methodology, which is considered as a reliable approach for distinguishing between live, early apoptotic, and late apoptotic or necrotic cells. The key aspect of this technique involves the externalization of phosphatidylserine (PS) during apoptosis, which facilitates the binding and visualization

of Annexin V through green fluorescence. To improve the specificity of the assay, Annexin V fluorescence was collected with a 525 nm band-pass filter (FL1 detector), while Propidium Iodide fluorescence was collected through a 620 nm band-pass filter (FL3 detector). This setup ensured precise quantification of apoptotic and necrotic cells, allowing for a comprehensive understanding of the compound's impact on cell viability.

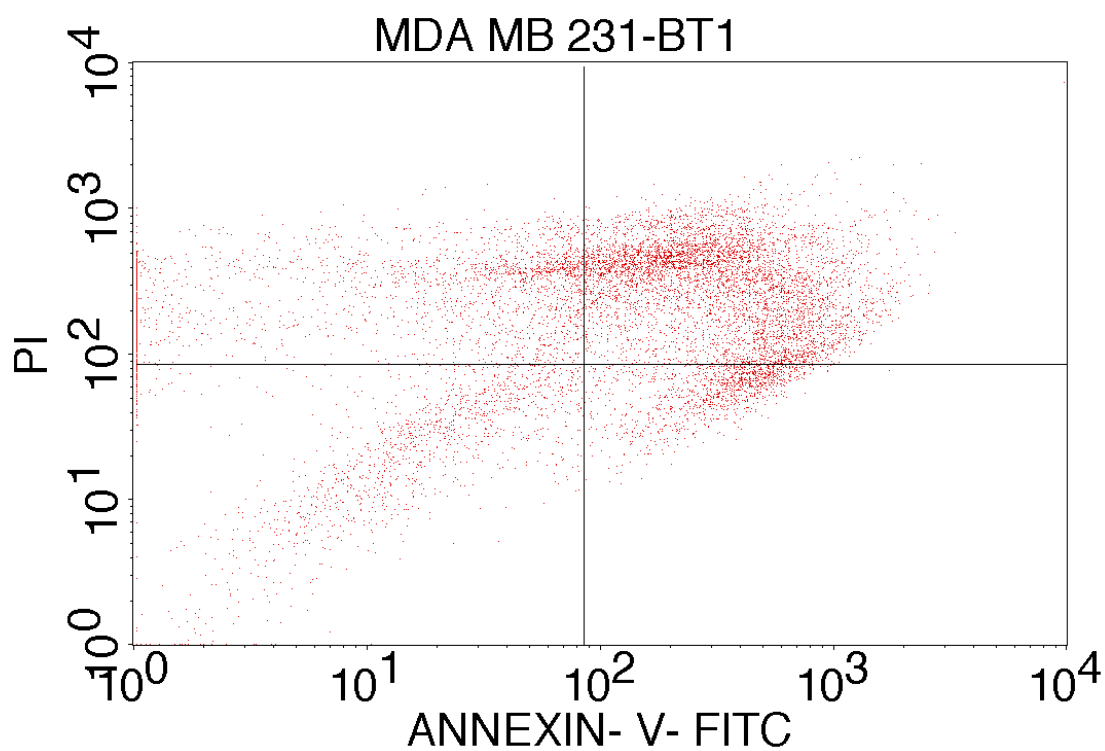
A significant modification in cell population distribution at various apoptosis stages was observed in MDA-MB-231 cells when exposed to the test compound **8a** at its IC<sub>50</sub> concentration (**Figure 9**). There was a significant increase in the early apoptotic population when compared to the control (untreated) cells, which was strongly associated with a noticeable rise in the percentage of Annexin V-positive and PI-negative cells. The enhanced mean fluorescence intensity (MFI) of the AbFlour 488 signal showed a higher presence of PS on the outer membrane of the treated cells, which correlated with the increase in early apoptotic cells.

It is noteworthy that the apoptosis assay results are consistent with the cell cycle analysis, which demonstrated a prominent G2/M phase arrest. The accumulation of cells in the G2/M phase indicates a cellular response to DNA damage or stress, potentially leading to the activation of apoptotic pathways in case the damage is irreversible. The increase observed in the SubG1 population during the cell cycle analysis, which suggests cells with damaged DNA, is likely to represent cells that are either on the pathway to apoptosis or have already undergone apoptotic cell death. The correlation between cell cycle arrest and apoptosis emphasizes the compound's capacity to initiate cell death by initially inhibiting cell division, specifically at the G2/M checkpoint, followed by apoptosis.

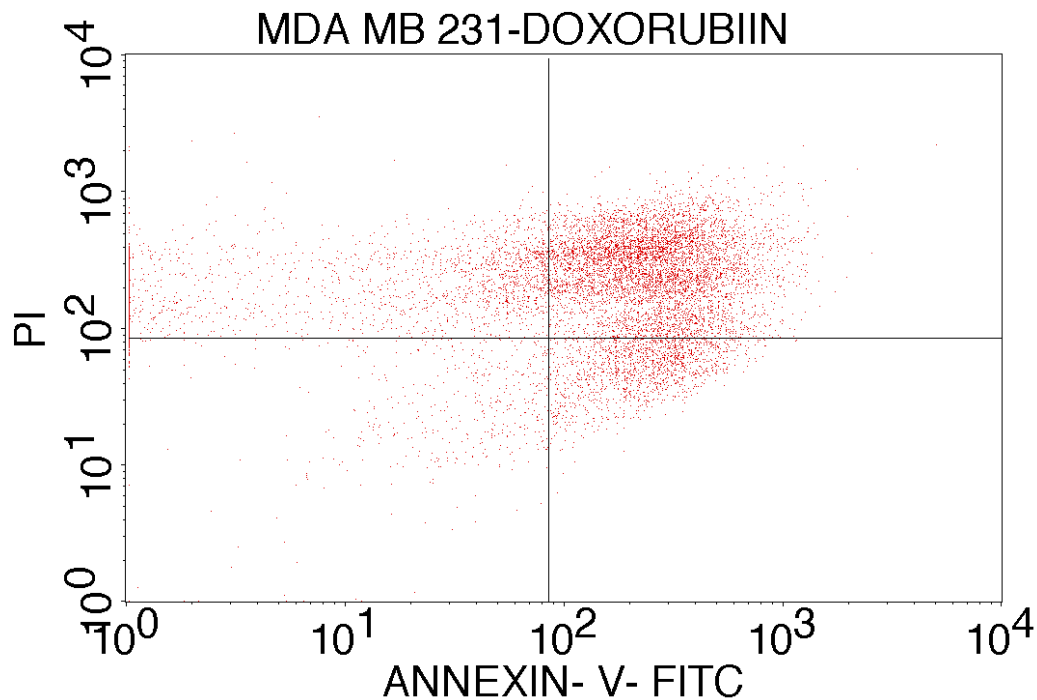
(a)



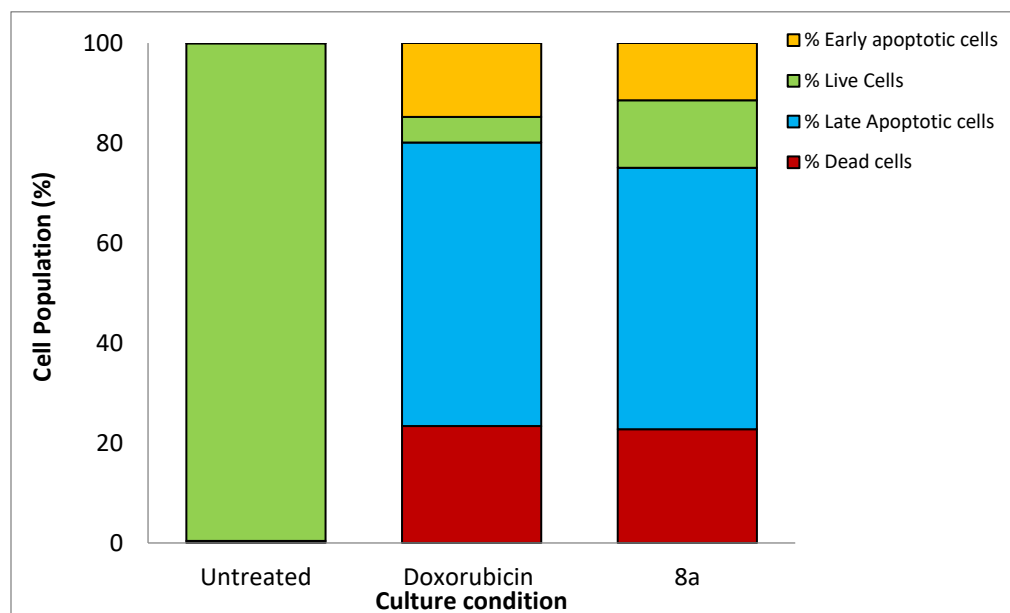
(b)



(c)



(d)



UL – Upper left: % of Necrotic Cells	UR – Upper right: % Late Apoptotic Cells
--------------------------------------	--

LL – Lower left: % Viable Cells	LR – Lower right: % of Early apoptotic cells
---------------------------------	--

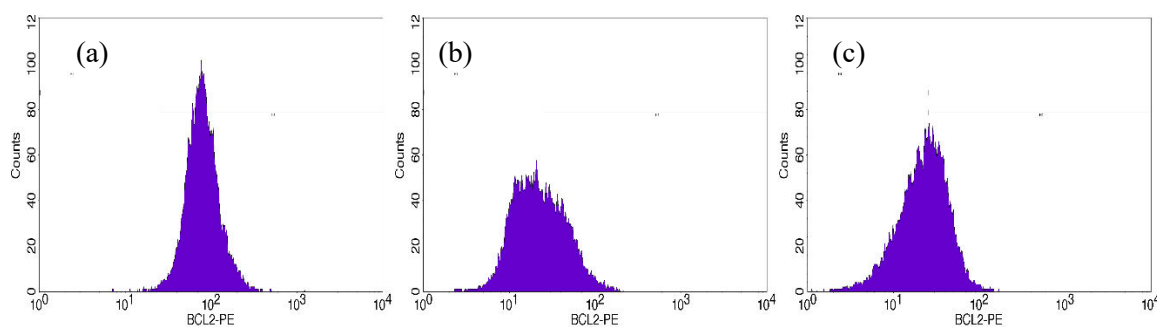
**Figure 9:** (a), (b) and (c) Quadrangular plots represented the Annexin V/PI expression in MDA MB 231 cells in the presence and absence of 8a and Std control by Flow Cytometry. Acquisition was done by using BD FACS Calibur and data analyzed by BD Cell Quest Pro Software (Version: 6.0) (d) Bar graph represented the % apoptotic cells in treated and untreated conditions of MDA MB 231 cells by Flow cytometry

Additionally, the data revealed a considerable increase in the late apoptotic/necrotic population, as evidenced by the co-expression of Annexin V and PI. These findings align with the cell cycle data, suggesting a disruption in cell cycle progression resulting in cell death. The drop in the G0/G1 phase population and the corresponding rise in both G2/M and SubG1 phases in the cell cycle analysis further support this apoptotic induction, as cells unable to progress past the G2/M checkpoint are more likely to undergo apoptosis. The observed apoptosis, particularly the significant induction of early apoptotic cells, suggests that the compound effectively disrupts cellular homeostasis, leading to a failure in mitosis and ultimately cell death. In brief, the data obtained from the apoptosis assay not only validate the compound's cytotoxic effects but also complement the cell cycle findings, offering a comprehensive insight into how the compound disrupts cancer cell proliferation.

### 3.2.6 Fluorescence-Activated Cell Sorting (FACS)- Bcl-2 expression study

Bcl-2 (B-cell lymphoma) is a critical protein that prevents programmed cell death, specifically in malignant cells, promoting their survival and proliferation. The levels of Bcl-2 expression in MDA-MB-231 cells were assessed using flow cytometry, which quantifies specific protein levels within individual cells. In this study, cells were stained using fluorophore-labeled antibodies (Bcl2-PE) and subsequently analyzed using the FACS method. The data is showcased through scatter plots and histograms, providing a comprehensive analysis of Bcl-2 expression under various treatment conditions, encompassing untreated cells, cells treated with a standard compound (doxorubicin), and cells treated with compound **8a**.

The histograms (Figure 10a, 10b, 10c) depict the distribution of cells according to the fluorescence intensity of Bcl-2-PE, with the M1 and M2 gates marking distinct fluorescence intensity ranges. M1 typically denotes cells with negative or low Bcl-2 expression, while M2 captures cells with positive or higher Bcl-2 expression, which is the focus of this analysis. The accompanying text to Figure 1 clarifies that the study specifically focuses on the percentage of cells within the M2 region, where positive Bcl-2 expression is observed. It is noted that gating into M1 and M2 is approximate and can be refined using Cell Quest Software, Version 6.0, allowing for more precise analysis.



(d)

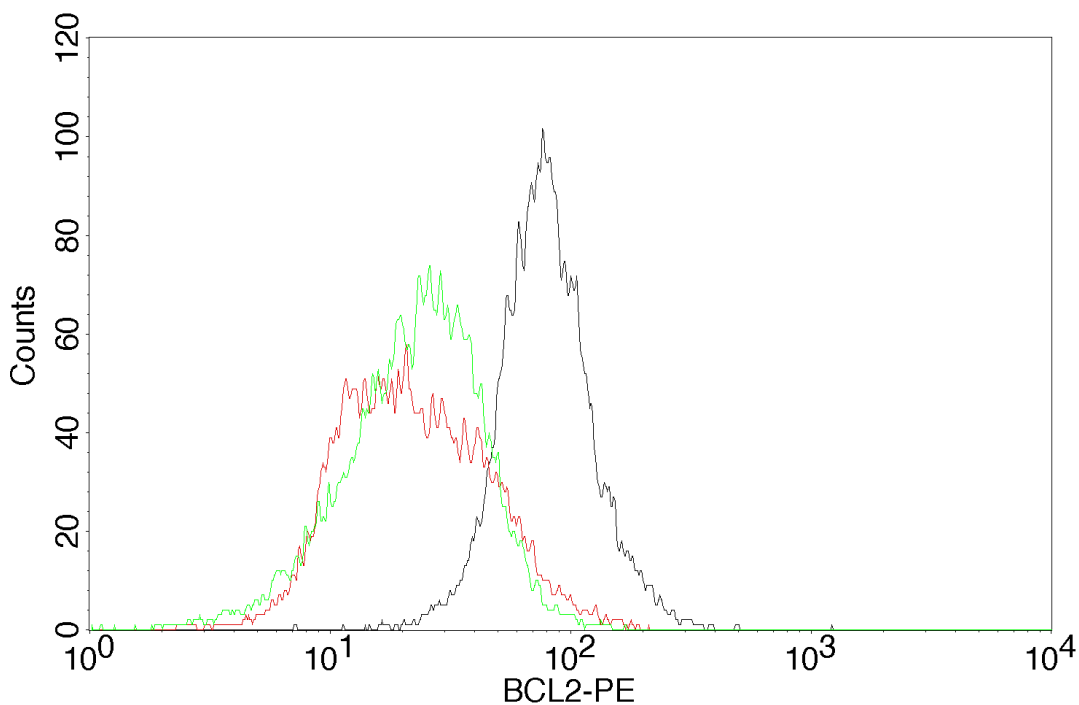
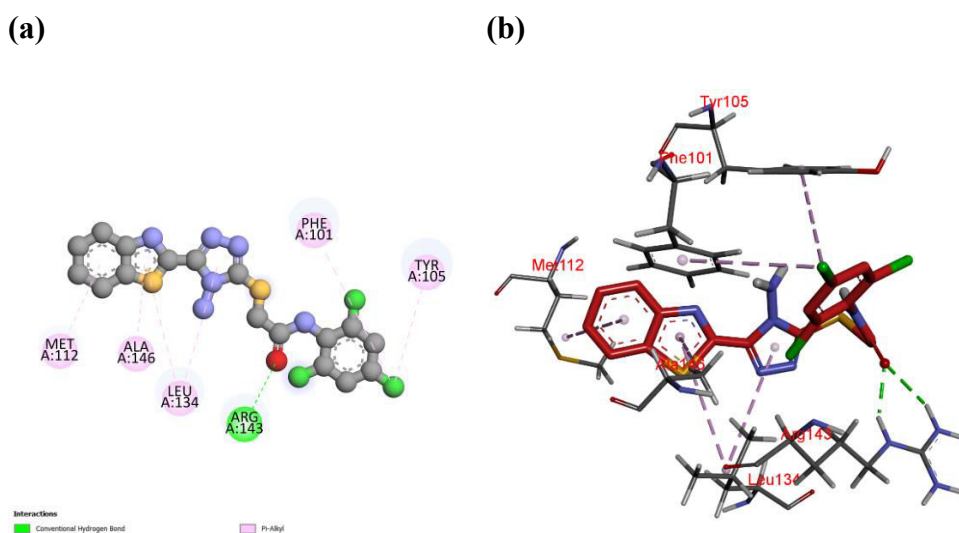


**Figure 10:** (a) Histogram of untreated cells with bcl-2 expression (b) Bcl-2 expression when treated with doxorubicin (c) effect of bcl-2 expression when treated with compound 8a (d) Montage histogram for comparative analysis for expression of bcl-2 protein

### 3.2.7 *In silico* Molecular Docking Studies on Bcl-2 Protein

To explore the binding interactions between the synthesized compound 8d, the standard chemotherapeutic agent doxorubicin, and the Bcl-2 protein, molecular docking studies were carried out. The crystal structure of Bcl-2 was acquired from the Protein Data Bank (PDB) under the code 4LVT. This structure was determined through X-ray crystallography with a resolution of 2.05 Å. The high-resolution structure served as a reliable framework for the assessment of the binding affinities and interaction patterns of the compounds.

The binding pocket was selected using the Protein Plus server and the DoGSiteScorer tool, which employs a grid-based approach using a difference of the Gaussian filter.<sup>196</sup> This method detects potential binding pockets based solely on the protein's 3D structure and then splits them into sub-pockets.<sup>197</sup> The identified binding pocket had a volume of 339.90 Å<sup>3</sup>, a surface area of 452.91 Å<sup>2</sup>, and a depth of 16.25 Å, with an ellipsoid main axis ratio of 0.11 (c/a) and 0.31 (b/a), indicating a moderately elongated pocket shape. The enclosure score of 0.30 suggests a partially enclosed binding environment, which can favor selective ligand interactions. The amino acid composition of the pocket included key residues, such as Ala, Arg, Asn, Asp, Gly, Leu, Phe, Trp, Tyr, and Val, highlighting its hydrophobic and polar interaction potential.



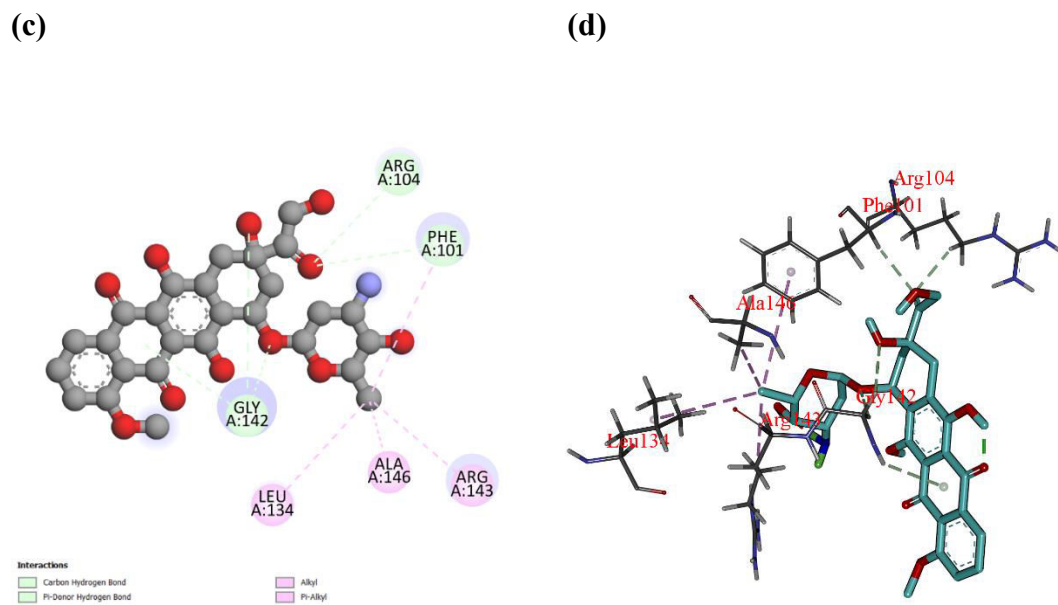


**Figure 11:** Docking interactions of molecule **8a** and doxorubicin with Bcl-2 (a) 2D interactions of **8a** within the Bcl-2 binding pocket (b) 3D interactions of **8a** showing key binding residues (c) 2D interactions of doxorubicin illustrating binding orientation (d) 3D interactions of doxorubicin highlighting key contact residues

The results of docking simulations showed molecule **8a** displayed a higher binding affinity to Bcl-2, with a binding energy of  $-7.6$  kcal/mol, in contrast to doxorubicin's binding energy of  $-7.3$  kcal/mol. The docking analysis revealed that **8a** interacts extensively with residues in the Bcl-2 binding pocket, leading to stronger binding and potential inhibitory effects (**Figures 11a and 11b**). The significant downregulation of Bcl-2 expression is probably a result of compound **8a** strong binding interactions, which stabilize the ligand within the pocket, as confirmed by in vitro flow cytometry assays. The correlation observed between the docking results and the decrease in Bcl-2 levels implies that **8a** effectively interfere with the anti-apoptotic role of Bcl-2 by occupying its binding site, thus facilitating apoptosis in cancer cells.

### 3.2.8 Molecular Dynamics and MM-PBSA Analysis of **8a** Interaction with Bcl-2

The stability and binding behavior of the Bcl-2 protein complexed with compound **8d** was elucidated through MD simulations over a 100 ns timescale, providing valuable insights. To understand the stability of the mentioned protein-ligand complex, the average values of



RMSD, RMSF, Radius of Gyration, and SASA were calculated and are presented in **Table 3**.

**Table 3:** Average RMSD, RMSF, Radius of Gyration, SASA and H-bonds values for the Protein-Ligand Complex of Bcl-2 and compound 8a

Average RMSD (nm)	Average RMSF (nm)	Average Radius of gyration (nm)	Average SASA (nm <sup>2</sup> )	Average H-bonds (count)
0.251	0.154	1.898	134.69	9

The consistent RMSD values indicate that **8a** effectively binds to Bcl-2, resulting in early stabilization and a disruption of its function. The consistent radius of gyration supports the stable interaction, suggesting that **8a** binding alters but maintains the protein structure, potentially hindering Bcl-2 anti-apoptotic function. The MD simulations reveal a decrease in solvent-accessible surface area (SASA), showing a structural compaction caused by molecule **8a** binding, which may lead to a conformational change that reduces the exposure to crucial anti-apoptotic regions. This structural alteration could disrupt the normal interaction sites of Bcl-2, thus inhibiting its protective effects against apoptosis. The presence of a stable hydrogen bonding pattern throughout the simulation further strengthens the role of compound **8d** in disrupting Bcl-2 function.

The MM-PBSA (Molecular Mechanics Poisson-Boltzmann Surface Area) analysis (**Table 4**) provided a detailed quantitative evaluation of the binding interactions, offering insights into the molecular forces driving molecule **8a** inhibition of Bcl-2. The significant van der Waals contributions emphasize the importance of hydrophobic interactions in stabilizing the complex. These interactions play a critical role by facilitating **8a**'s integration into the hydrophobic pockets of Bcl-2, preventing the protein from interacting with its pro-survival partners. Furthermore, the important electrostatic contributions suggest that molecule **8a** establishes vital charge-based interactions, improving the specificity and strength of binding. These electrostatic interactions may involve key residues that are pivotal for Bcl-2's function, directly disrupting its anti-apoptotic signaling. The positive polar solvation energy observed is counterbalanced by the strong van der Waals and electrostatic

interactions, resulting in a favorable overall binding free energy. This balance underscores the specificity of **8a** for the Bcl-2 binding pocket, which is critical for selective inhibition. The MM-PBSA binding free energy of **8a** indicates a significant and specific potential for inhibition, which directly corresponds to the observed downregulation of in vitro Bcl-2 expression.

**Table 4:** MM-PBSA Free Energy Calculation Results for the compound **8d** and Bcl-2 Complex

Energy components	Values (kJ/mol)
$\Delta E_{vdW}$	$-360.327 \pm 16.120$ kJ/mol
$\Delta E_{elec}$	$-63.722 \pm 8.920$ kJ/mol
$\Delta E_{polar}$	$308.098 \pm 24.961$ kJ/mol
$\Delta E_{SASA}$	$-34.589 \pm 0.925$ kJ/mol
$\Delta E_{SAV}$	$0.000 \pm 0.000$ kJ/mol
$\Delta E_{WCA}$	$0.000 \pm 0.000$ kJ/mol
$\Delta G_{bind}$	$-150.541 \pm 30.763$ kJ/mol

$\Delta E_{vdW}$ : van der Waals energy contribution,  $\Delta E_{elec}$ : Electrostatic energy contribution,  $\Delta E_{polar}$ : Polar solvation energy contribution,  $\Delta E_{SASA}$ : Solvent-accessible surface area energy contribution,  $\Delta E_{SAV}$ : Solvent-accessible volume energy contribution,  $\Delta E_{WCA}$ : Water-cavity area energy contribution,  $\Delta G_{bind}$ : Total binding free energy of the complex

By establishing strong and stable inhibitory interactions, molecule **8a** effectively disrupts the anti-apoptotic function of Bcl-2, leading to increased cell susceptibility to apoptosis. The correlation between these molecular insights and the in vitro Bcl-2 expression studies offers a comprehensive understanding of **8a**'s mechanism of action. The MD simulations showed consistent stability in the structure and energy of compound **8a**. This, along with the finding of reduced Bcl-2 expression, suggests that **8a** has great potential as a powerful inhibitor of Bcl-2. This highlights its promise in TNBC therapy by inducing apoptosis in cancer cells that overexpress Bcl-2.

### 3.3 Material and methods

#### 3.3.1 Chemistry

All the chemicals and reagents used were of analytical grade and did not require any further purification. 2-Aminothiophenol (CAS No: 137-07-5) and diethyl oxalate (CAS No: 95-92-1) were acquired from Spectrochem. Carbon disulfide (CAS No: 75-15-0) and hydrazine hydrate (99%) (CAS No: 7803-57-8) were acquired from CDH. Potassium hydroxide (CAS No: 1310-58-3) and sodium hydroxide (CAS No: 1310-73-2) were purchased from Molychem. Thin-layer chromatography (TLC) was carried out using Silica Gel 60 F254 TLC Aluminum Sheets (Merck KGaA, Darmstadt, Germany), and spots were visualized under UV light at 254 nm and 365 nm. <sup>1</sup>H NMR (400 MHz) and <sup>13</sup>C NMR (101 MHz) spectra were recorded on an AvanceNeo Ascend spectrometer in DMSO-*d*<sub>6</sub>, with chemical shifts reported in δ ppm relative to TMS. Mass spectra were obtained using a Waters ACQUITY QDa spectrometer with a direct inlet method. FT-IR spectra were recorded on a Shimadzu FTIR-8400 spectrometer using the KBr pellet method. Melting points were measured on an electrothermal device from Tempo Instruments using open capillaries and are uncorrected.

- **Standard protocol for the synthesis of benzothiazole-2-carboxylate (3)**

The mixture of diethyl oxalate **1** (20 mmol) and 2-aminothiophenol **2** (10 mmol) was refluxed for 5 hours. Confirmation of the reaction completion was done through TLC, using ethyl acetate and n-hexane (2:1). The mixture was subjected to cooling and then stirred with 50 mL of methanol for 30 minutes. It was subsequently poured into a solution of 20 mL of HCl and 80 mL of water, which was vigorously stirred. The resulting white solid was separated by vacuum filtration, dried, and recrystallized from methanol, yielding benzothiazole-2-carboxylate **3** as a white solid in 94% yield.

- **Standard procedure for synthesis of benzothiazole-2-carbohydrazide (4)**

Benzothiazole-2-carboxylate **3** (10 mmol) was solubilized in 50 mL of absolute ethanol. Drop-wise addition of hydrazine hydrate (99%) was carried out in this solution, which was then refluxed for a period of 6 hours. The progress of the reaction was monitored by TLC, using a solvent mixture of ethyl acetate and n-

hexane at a ratio of 2:1. Following the completion of the reaction, the mixture was cooled to room temperature, subjected to vacuum filtration, rinsed with water, and left to dry overnight. The process resulted in an 86% yield of yellow benzothiazole-2-carbohydrazide **4**.

○ **General method for Synthesis of potassium 2-(benzo[d]thiazole-2-carbonyl) hydrazine-1-carbodithioate salt (5)**

The compound Benzothiazole-2-carbohydrazide **4** (10 mmol) was dissolved in a methanolic solution of potassium hydroxide (15 mmol) and underwent stirring at room temperature. The mixture was then subjected to dropwise addition of carbon disulfide (15 mmol), followed by continuous stirring for 18 hours. The completion of the reaction was validated through TLC. Subsequently, the reaction mixture underwent vacuum filtration, and the resultant solid was subjected to multiple washes with diethyl ether. The product was dried in an oven at 80°C for 3 hours. A yellow salt of potassium 2-(benzo[d]thiazole-2-carbonyl) hydrazine-1-carbodithioate **5** was obtained with a 92% yield. This salt was used without additional purification in the subsequent reaction.

○ **Synthesis of 4-amino-5-(benzo[d]thiazol-2-yl)-4H-1,2,4-triazole-3-thiol moiety (6)**

The first step was to dissolve 10 mmol of potassium dithiocarbazinate salt **5** in water, and then hydrazine hydrate (99%, 20 mmol) was added dropwise to the solution. The mixture was heated to 90°C under reflux conditions. As the reaction progressed, hydrogen sulfide gas was released and its existence was confirmed by the color change of a filter paper soaked in lead acetate, which turned from white to black. Once the evolution of hydrogen sulfide gas was complete, the reaction mixture was cooled down to room temperature, followed by a workup using a 20% HCl solution in water. The slight yellow precipitate that formed was collected through vacuum filtration, then washed with hot ethanol, and finally dried in an oven at 100°C. This process produced pure 4-amino-5-(benzo[d]thiazol-2-yl)-4H-1,2,4-triazole-3-thiol **6** as a white solid. Yield 90%; White solid; mp: 221-223 °C; <sup>1</sup>H NMR (400 MHz, DMSO-*d*<sub>6</sub>): δ 14.38 (s, 1H, SH), 8.29–8.22 (d, 1H, Ar–H), 8.21–8.14 (d, 1H, Ar–H), 7.61 (dddd, J = 22.4, 8.4, 7.2, 1.3 Hz, 2H, Ar–H), 6.19 (s,

2H, NH<sub>2</sub>); <sup>13</sup>C NMR (101 MHz, DMSO-*d*<sub>6</sub>) δ 167.36 (C–SH), 152.55 (C–C), 144.94 (C–C), 152.49, 135.15, 127.52, 127.14, 124.05, 122.91 (Ar–C); (ESI-MS) *m/z* 249.90 (M+H)<sup>+</sup>.

○ **Standard procedure for synthesis of 2-chloro-N-phenylacetamide derivatives (7a-e)**

Aniline derivatives **9a-e** (10 mmol) were dissolved in acetone, and potassium carbonate (15 mmol) was added to the solution. The mixture was stirred for 30 minutes to ensure complete dissolution. Subsequently, chloroacetyl chloride (12 mmol) was added dropwise to the stirred solution, and the reaction was allowed to proceed at room temperature for 3 hours. The completion of the reaction was monitored using TLC. Upon completion, the resulting precipitate was collected by vacuum filtration, washed thoroughly with excess water and dried. The product, 2-chloro-N-phenylacetamide **7a-e** derivatives, were obtained as a solid and used directly in subsequent reactions without further purification.

○ **General procedure for synthesis of 2-((4-amino-5-(benzo[d]thiazol-2-yl)-4H-1,2,4-triazol-3-yl)thio)-N-phenylacetamide derivatives (8a-e)**

Benzothiazole tethered triazole moiety **6** (10 mmol) was added to 20 mL of methanol and sonicated for 5 minutes to ensure proper dispersion. Sodium hydroxide (10 mmol) was then added to the suspension, and the mixture was stirred at room temperature until all reactants were fully dissolved. After stirring for 30 minutes, N-phenylacetamide derivatives **7a-e** (11 mmol) were introduced to the solution, and the reaction was allowed to proceed at room temperature. The reaction mixture led to the formation of precipitates, which were collected by vacuum filtration, washed thoroughly with water, and dried overnight at room temperature. To obtain pure 2-((4-amino-5-(benzo[d]thiazol-2-yl)-4H-1,2,4-triazol-3-yl)thio)-N-phenylacetamide derivatives **8a-e**, the solid product was further washed with hot ethanol.

○ **2-((4-amino-5-(benzo[d]thiazol-2-yl)-4H-1,2,4-triazol-3-yl)thio)-N-(2,4,6-trichlorophenyl)acetamide (8a)**

Yield 83%; White solid; mp 236-238 °C; FT-IR (KBr, ν, cm<sup>-1</sup>): 3248.23 (NH<sub>2</sub> stretch), 3178.79 (-NH- stretch), 1689.70 (C=O stretch); <sup>1</sup>H NMR (400 MHz,

DMSO-*d*<sub>6</sub>):  $\delta$  10.16 (s, 1H, NH), 8.24 (d, *J* = 8.0 Hz, 1H, Ar-H), 8.17–8.14 (d, *J* = 10.5 Hz, 2H, Ar-H), 7.93 (s, 1H, Ar-H), 7.64–7.54 (m, 2H, Ar-H), 6.57 (s, 2H, NH<sub>2</sub>), 4.33 (s, 2H, CH<sub>2</sub>); <sup>13</sup>C NMR (101 MHz, DMSO-*d*<sub>6</sub>):  $\delta$  167.00 (C=O), 154.78 (N=C), 154.39 (C-S), 152.78 (NS-C), 148.79 (C-C), 134.83, 130.58, 129.88, 127.16, 126.98, 126.57, 125.07, 124.52, 123.41, 122.50, 35.06 (CH<sub>2</sub>); (ESI-MS) *m/z* 486 (M+H)<sup>+</sup>; Anal. Calcd for C<sub>17</sub>H<sub>11</sub>Cl<sub>3</sub>N<sub>6</sub>OS<sub>2</sub>: C, 42.03; H, 2.28; N, 17.30; Found: C, 42.01; H, 2.23; N, 17.24%.

○ **2-((4-amino-5-(benzo[d]thiazol-2-yl)-4H-1,2,4-triazol-3-yl)thio)-N-(4-bromophenyl)acetamide (8b)**

Yield 88%; White solid; mp 203-205 °C; FT-IR (KBr,  $\nu$ , cm<sup>-1</sup>): 3263.66 (NH<sub>2</sub> stretch), 3163.36 (-NH- stretch), 1651.12 (C=O stretch); <sup>1</sup>H NMR (400 MHz, DMSO-*d*<sub>6</sub>)  $\delta$  10.53 (s, 1H, NH), 8.28–8.20 (m, 1H, Ar-H), 8.20–8.14 (m, 1H, Ar-H), 7.64–7.50 (m, 6H, Ar-H), 6.56 (s, 2H, NH<sub>2</sub>), 4.25 (s, 2H, CH<sub>2</sub>); <sup>13</sup>C NMR (101 MHz, DMSO-*d*<sub>6</sub>)  $\delta$  165.88 (C=O), 154.97 (N=C), 154.45 (C-S), 152.79 (NS-C), 148.71 (C-C), 138.19, 133.78, 131.62, 127.29, 126.97, 126.54, 123.39, 122.49, 121.02, 115.05, 35.52 (CH<sub>2</sub>); (ESI-MS) *m/z* 460.10 (M+H)<sup>+</sup>; Anal. Calcd for C<sub>17</sub>H<sub>13</sub>BrN<sub>6</sub>OS<sub>2</sub>: C, 44.26; H, 2.84; N, 18.22; Found: C, 44.23; H, 2.83; N, 18.19%.

○ **2-((4-amino-5-(benzo[d]thiazol-2-yl)-4H-1,2,4-triazol-3-yl)thio)-N-(4-fluorophenyl)acetamide (8c)**

Yield 87%; White solid; mp 202-204 °C; FT-IR (KBr,  $\nu$ , cm<sup>-1</sup>): 3271.38 (NH<sub>2</sub> stretch), 3155.65 (-NH- stretch), 1651.12 (C=O stretch); <sup>1</sup>H NMR (400 MHz, DMSO-*d*<sub>6</sub>)  $\delta$  10.45 (s, 1H, NH), 8.28–8.20 (m, 1H, Ar-H), 8.16–8.14 (m, 1H, Ar-H), 7.67–7.60 (m, 3H, Ar-H), 7.58–7.54 (td, *J* = 7.6, 1.3 Hz, 1H, Ar-H), 7.19–7.14 (m, 2H, Ar-H), 6.56 (s, 2H, NH<sub>2</sub>), 4.24 (s, 2H, CH<sub>2</sub>); <sup>13</sup>C NMR (101 MHz, DMSO-*d*<sub>6</sub>)  $\delta$  165.63 (C=O), 154.70 (N=C), 154.50 (C-S), 154.28 (C-F), 152.78 (NS-C), 148.62 (C-C), 135.16, 133.83, 127.34, 126.95, 126.53, 123.40, 122.43, 121.10, 115.41, 115.20, 35.62 (CH<sub>2</sub>); (ESI-MS) *m/z* 400 (M+H)<sup>+</sup>; Anal. Calcd for C<sub>17</sub>H<sub>13</sub>FN<sub>6</sub>OS<sub>2</sub>: C, 50.99; H, 3.27; N, 20.99; Found: C, 50.91; H, 3.22; N, 20.96%.

○ **2-((4-amino-5-(benzo[d]thiazol-2-yl)-4H-1,2,4-triazol-3-yl)thio)-N-(2,6-dimethylphenyl)acetamide (8d)**

Yield 91%; White solid; mp 221-223 °C; FT-IR (KBr,  $\nu$ ,  $\text{cm}^{-1}$ ): 3263.66 ( $\text{NH}_2$  stretch), 3039.91 (-NH- stretch), 1658.84 (C=O stretch);  $^1\text{H}$  NMR (400 MHz, DMSO- $d_6$ )  $\delta$  9.66 (s, 1H, NH), 8.24–8.22 (m, 1H, Ar-H), 8.16–8.14 (m, 1H, Ar-H), 7.64–7.54 (dddd,  $J = 23.6, 8.4, 7.2, 1.3$  Hz, 2H, Ar-H), 7.07–7.05 (m, 3H, Ar-H), 6.56 (s, 2H,  $\text{NH}_2$ ), 4.25 (s, 2H,  $\text{CH}_2$ ), 2.13 (s, 6H,  $(\text{CH}_3)_2$ );  $^{13}\text{C}$  NMR (101 MHz, DMSO- $d_6$ )  $\delta$  165.44 (C=O), 154.88 (N=C), 154.42 (C-S), 152.75 (NS-C), 148.72 (C-C), 135.17, 134.67, 133.80, 127.63, 126.98, 126.54, 123.39, 122.50, 34.59 ( $\text{CH}_2$ ), 17.99 ( $\text{CH}_3$ )<sub>2</sub>; (ESI-MS)  $m/z$  : 410.05 ( $\text{M}+\text{H}$ )<sup>+</sup>; Anal. Calcd for  $\text{C}_{19}\text{H}_{18}\text{N}_6\text{OS}_2$ : C, 55.59; H, 4.42; N, 20.47; Found: C, 55.58; H, 4.40; N, 20.46%.

○ **2-((4-amino-5-(benzo[d]thiazol-2-yl)-4H-1,2,4-triazol-3-yl)thio)-N-(p-tolyl)acetamide (8e)**

Yield 93%; White solid; mp 227-229 °C; FT-IR (KBr,  $\nu$ ,  $\text{cm}^{-1}$ ): 3263.66 ( $\text{NH}_2$  stretch), 3163.36 (-NH- stretch), 1658.84 (C=O stretch);  $^1\text{H}$  NMR (400 MHz, DMSO)  $\delta$  10.31 (s, 1H, NH), 8.22 (d, 1H, Ar-H), 8.15 (d, 1H, Ar-H), 7.50 (d, 4H, Ar-H), 7.12 (m, 2H, Ar-H), 6.57 (s, 2H,  $\text{NH}_2$ ), 4.25 (s, 2H,  $\text{CH}_2$ ), 2.25 (s, 3H,  $\text{CH}_3$ );  $^{13}\text{C}$  NMR (101 MHz, DMSO)  $\delta$  165.90 (C=O), 155.60 (N=C), 154.97 (C-S), 153.28 (NS-C), 149.19 (C-C), 136.84, 134.28, 132.91, 129.66, 127.46, 127.02, 123.89, 122.98, 119.58, 36.09 ( $\text{CH}_2$ ), 20.93 ( $\text{CH}_3$ ); (ESI-MS)  $m/z$  : 396.05 ( $\text{M}+\text{H}$ )<sup>+</sup>; Anal. Calcd for  $\text{C}_{18}\text{H}_{16}\text{N}_6\text{OS}_2$ : C, 54.53; H, 4.07; N, 21.20; Found: C, 54.52; H, 4.01; N, 21.19%.

### 3.3.2 One-Dose Screening Assay Procedure

In the NCI DTP-60 program, the synthesized compounds were subjected to a one-dose screening assay to assess their anticancer potential.<sup>198,199,200</sup> A concentration of 10  $\mu\text{M}$  was used to test each compound against a diverse panel of approximately 60 human cancer cell lines, encompassing a range of cancer types such as leukemia, melanoma, lung, colon, brain, ovary, breast, prostate, and kidney cancers. The compounds were prepared through dissolution in a mixture of DMSO and glycerol in a 9:1 ratio to attain the desired concentration. The cell lines were cultured following standard protocols, wherein cells were seeded into 96-well plates and allowed to adhere overnight. Then, the test compound

was added to each well and left to incubate for a period of 48 hours. Cell viability was examined after the incubation period using a relevant assay, such as sulforhodamine B (SRB), which measures the total protein content or metabolic activity as an indicator of cell growth and viability. By comparing the treated wells to the untreated controls, the percentage of cell growth inhibition was calculated. This method allowed for the identification of both growth inhibitory and cytotoxic effects. Compounds that demonstrate significant growth suppression at this point could be identified as potential candidates for further studies as anticancer agents.

### 3.3.3 MTT Assay

The MTT assay, a widely used colorimetric assay for measuring cellular proliferation and viability, was used to assess the cytotoxic effects of the synthesized compounds on the MDA-MB-231 breast cancer cell line obtained from NCCS, Pune, India.<sup>201,202</sup> Cells were maintained in DMEM high glucose medium (Gibco, Cat No: 12430), supplemented with 10% fetal bovine serum (Himedia, Cat No: RM10432) and 1% antibiotic-antimycotic solution, at 37°C with 5% CO<sub>2</sub> in a humidified atmosphere. The cells were sub-cultured every 48 hours, and those at passage 39 were utilized for the experiments. The assay involved seeding cells at a density of 20,000 cells per well in 200 µL of medium in 96-well plates, followed by a 24-hour incubation period for attachment. Following that, the cells were subjected to various concentrations of the test compounds and kept in the same conditions for an extra 24 hours. The media was removed after incubation, and then 0.5 mg/mL of MTT reagent (Himedia, Cat No: 4060) was introduced to each well. In order to prevent light interference, the plates were wrapped in aluminum foil and left to incubate for 3 hours, allowing formazan crystals to form.<sup>203</sup> Following incubation, the MTT reagent was cautiously extracted, and then 100 µL of DMSO (Sigma, Cat No: PHR1309) was introduced to dissolve the formazan crystals. To ensure the thorough dissolution, the plates were gently agitated on a gyratory shaker. The absorbance was measured at a wavelength of 570 nm using a BioRad microplate spectrophotometer (Model: xMark Microplate Absorbance Spectrophotometer, Cat No: 1681150). Cell viability was calculated using the formula:



$$\%cell\ viability = \frac{\text{mean absorbance of treated cells}}{\text{mean absorbance of untreated cells}} \times 100$$

The IC<sub>50</sub> values were determined from the viability curves using linear regression (Y = Mx + C), where Y is 50% viability.

### 3.3.4 Flow Cytometric Analysis of Cell Cycle

The effect of the synthesized compound on the cell cycle distribution of MDA-MB-231 cells was assessed through flow cytometry analysis.<sup>204</sup> MDA-MB-231 cells, sourced from NCCS Pune, were cultured in 6-well plates with a cell density of  $2 \times 10^5$  cells per well in 2 mL of culture medium.<sup>205</sup> The cells were then incubated at 37°C in a 5% CO<sub>2</sub> atmosphere for 24 hours. After the incubation period, the spent medium was aspirated, and the cells were washed with 1 mL of 1X phosphate-buffered saline (PBS). The test compound was then applied to the cells at their respective IC<sub>50</sub> concentration, and incubated for another 24 hours in the same environment. Untreated cells served as the negative control. Cells were fixed by adding cold 70% ethanol dropwise to the cell pellet while vortexing, ensuring thorough fixation and minimizing clumping. The cells were fixed on ice for at least 30 minutes. After fixation, the cells were pelleted by centrifugation at higher speeds due to increased buoyancy post-fixation and then washed twice with 1X PBS to remove any residual ethanol. The cell pellets were resuspended in 400 µL of propidium iodide (PI) and RNase staining solution (BD Biosciences, Catalog no. 550825) per million cells. The mixture was then incubated at room temperature for 5 to 10 minutes. Sample was analyzed without additional washing using a Cytomics FC500 Flow cytometer (Beckman Coulter, USA). Data analysis was conducted using FlowJo X 10.0.7 software, which allowed for the quantification of cell populations in different phases of the cell cycle, providing insights into the impact of the test compound on cell cycle progression.

### 3.3.5 Annexin V Apoptosis Assay by Flow Cytometry

The evaluation of MDA-MB-231 cell apoptosis was conducted using the Annexin V-AbFlour™ 488 Apoptosis Detection Kit (KTA0002, Abbkine, Inc.) which detects the externalization of phosphatidylserine, a hallmark of early apoptosis with flow cytometry analysis.<sup>206,207</sup> MDA-MB-231 cells, acquired from NCCS Pune, were cultured in 6-well

plates, with each well containing  $0.5 \times 10^6$  cells in 2 mL of culture medium. The cells were then incubated at 37°C in a 5% CO<sub>2</sub> atmosphere for 24 hours. Once the incubation was completed, the medium was removed, and the cells were carefully rinsed with 1 mL of 1X phosphate-buffered saline (PBS, HiMedia). Subsequently, the cells were subjected to the desired concentration of the experimental test compound and incubated for an additional duration of 24 hours. An untreated well was used as the negative control. Post-treatment, the medium from each well was collected into 15 mL centrifuge tubes, and the cells were washed with 1 mL of PBS, which was also collected into the same tubes to ensure the capture of any non-adherent cells. The adherent cells were then treated with 0.5 mL of trypsin-EDTA solution (HiMedia) and incubated at 37°C for 3-4 minutes to detach the cells. The wells were replenished with the culture medium to neutralize the trypsin, and all the cells were harvested into their respective centrifuge tubes. Centrifugation of the cell suspensions was carried out at 300 x g for 5 minutes at a temperature of 25°C, followed by the careful decantation of the supernatant. The cell pellets were thoroughly rinsed with PBS, ensuring that all trypsin and leftover medium were eliminated. The cells were resuspended in 1X Binding Buffer (prepared by diluting 10X Binding Buffer with distilled water) at a concentration of  $1 \times 10^6$  cells/mL. A 100 µL aliquot of the cell suspension ( $1 \times 10^5$  cells) was transferred to a 5 mL culture tube. To this, 5 µL of AbFlour 488 Annexin V was added, and the cells were gently vortexed and incubated for 15 minutes at room temperature (25°C) in the dark to allow for Annexin V binding. After the incubation period, 2 µL of propidium iodide (PI) and 400 µL of 1X Binding Buffer were introduced into each tube. The cells were mixed gently and immediately analyzed using a Cytomics FC500 Flow Cytometer (Beckman Coulter, USA). To quantify the apoptotic populations, including live, early apoptotic, late apoptotic, and necrotic cells, the data was analyzed using FlowJo X 10.0.7 software.

### 3.3.6 FACS-Bcl2 expression studies

Bcl-2 protein expression was evaluated using MDA-MB-231 human breast adenocarcinoma cells (NCCS, Pune). The cells were cultured in DMEM high glucose medium (Gibco, Cat No: 11965-084) supplemented with 10% fetal bovine serum (Gibco, Cat No: 10270-106) and 1% antibiotic-antimycotic solution. The culture conditions were

maintained at a temperature of 37°C and a 5% CO<sub>2</sub> humidified atmosphere. The cells were sub-cultured every 72 hours, and the ones at passage 49 were used for experiments. The cells were seeded in 6-well plates, with each well containing a density of 0.5×10<sup>6</sup> cells in 2 mL of medium and incubated overnight. After 24 hours, the spent medium was aspirated, and the cells were treated with experimental compound at their IC<sub>50</sub> concentrations, along with control, including untreated well as negative control. After that, the cells were left to incubate for another 24 hours. After incubation, the medium was taken out, and the cells were rinsed with PBS. The cells were detached by adding a 200 µL aliquot of trypsin-EDTA solution and collected in 12x75 mm polystyrene tubes with 2 mL culture medium. The cell suspensions were centrifuged at 300 x g for 5 minutes at 25°C, and the supernatant was carefully decanted. The cells were fixed by dropwise addition of 1 mL of ice-cold 70% ethanol while vortexing to prevent clumping, and incubated on ice for at least 30 minutes. After fixation, the cells were centrifuged at higher speeds to pellet the fixed cells, then washed twice with PBS and subsequently with 0.5% BSA in PBS containing 0.1% sodium azide to decrease nonspecific binding. In order to detect Bcl-2 expression, 5 µL of PE-conjugated anti-Bcl-2 antibody (BioLegend, Cat No: 658707) was applied and the cells were then incubated at room temperature for 30 minutes in dark.<sup>208,209</sup> After staining, the cells were rinsed with PBS containing 0.1% sodium azide, suspended in 0.5 mL PBS, and examined using a BD FACS Calibur flow cytometer (BD Biosciences, USA) with excitation at 488 nm and emission at 578 nm (FL-2 channel). BD CellQuest Pro software (Version 6.0) was used to analyze the data, with a minimum of 10,000 cells counted for each sample.

### 3.3.7 Molecular docking procedure

Molecular docking was performed to evaluate the interactions between the synthesized compound, doxorubicin, and the Bcl-2 protein. The three-dimensional structure of Bcl-2 (PDB ID: 4LVT) was retrieved from the RCSB Protein Data Bank. To prepare the protein for docking, all water molecules and heteroatoms were removed using UCSF Chimera (version 1.17.3).<sup>210</sup> Protein preparation involved using Chimera's Dock Prep tool, where incomplete side chains were reconstructed using the Dunbrack 2010 rotamer library, ensuring the structural integrity of the protein.<sup>211</sup> Hydrogen atoms were added to optimize

the geometry for accurate interaction modeling, and electrostatic charges were assigned using AMBER ff14SB for standard residues and AM1-BCC for other residues to enable precise electrostatic calculations. The ligands were prepared using the ACPYPE server and the AMBER method with the bcc charge assignment to optimize their conformations and improve the accuracy of the docking process.<sup>212</sup> Docking simulations were conducted using AutoDock Vina 1.5.7, integrated as an extension in UCSF Chimera.<sup>213</sup> The docking parameters were set to limit binding modes to 10, exhaustiveness to 8, and maximum energy difference to 3 kcal/mol for favorable interactions. The top docking poses were analyzed and visualized using BIOVIA Discovery Studio Visualizer 2024 to study ligand-protein interactions.<sup>214</sup>

### 3.3.8 Molecular dynamics simulation

Molecular dynamics (MD) simulations were conducted using the GROMACS 2019.4 software package.<sup>215</sup> The ligand topology was generated using the Automated Topology Builder (ATB) server to ensure accurate force field parameters.<sup>216</sup> The system was prepared by performing vacuum minimization using the steepest descent algorithm for 1500 steps. Following minimization, the protein-ligand complex was solvated in a cubic periodic box with a distance of 0.5 nm between the complex and the box edges, utilizing the simple point charge (SPC) water model. To neutralize the system and achieve a physiological salt concentration, 0.15 M Na<sup>+</sup> and Cl<sup>-</sup> ions were added. The system preparation was performed following the methodology described in a previously published study (PMID: 31514687). After equilibration under an isothermal-isobaric (NPT) ensemble, the final production run was executed for 100 ns in the NPT ensemble. Trajectory analysis was performed using the GROMACS simulation tools, assessing root mean square deviation (RMSD), root mean square fluctuation (RMSF), radius of gyration (Rg), solvent-accessible surface area (SASA), and hydrogen bond interactions. The analysis procedures followed established protocols from previous studies (PMID: 32567989).

## 3.4 Conclusion

In summary, the synthesized compounds, which were composed of benzothiazole tethered triazole structures and N-phenyl acetamide chains, exhibited significant anticancer activity

when tested in vitro. This was evident through their ability to inhibit the viability of MDA-MB-231 cells. The results of the mechanistic studies indicate that the compounds possess the capability to induce G2/M cell cycle arrest, promote apoptosis, and downregulate Bcl-2 expression. Molecular docking and dynamics simulations provided additional evidence to support the compounds' potential as potent anticancer agents, showing their effective interaction with key cancer-related proteins. These findings strongly imply that the synthesized compounds possess great potential and could be further developed as effective therapeutic candidates for the treatment of cancer.

### 3.5 spectral data

➤ Spectral data of compound 8a

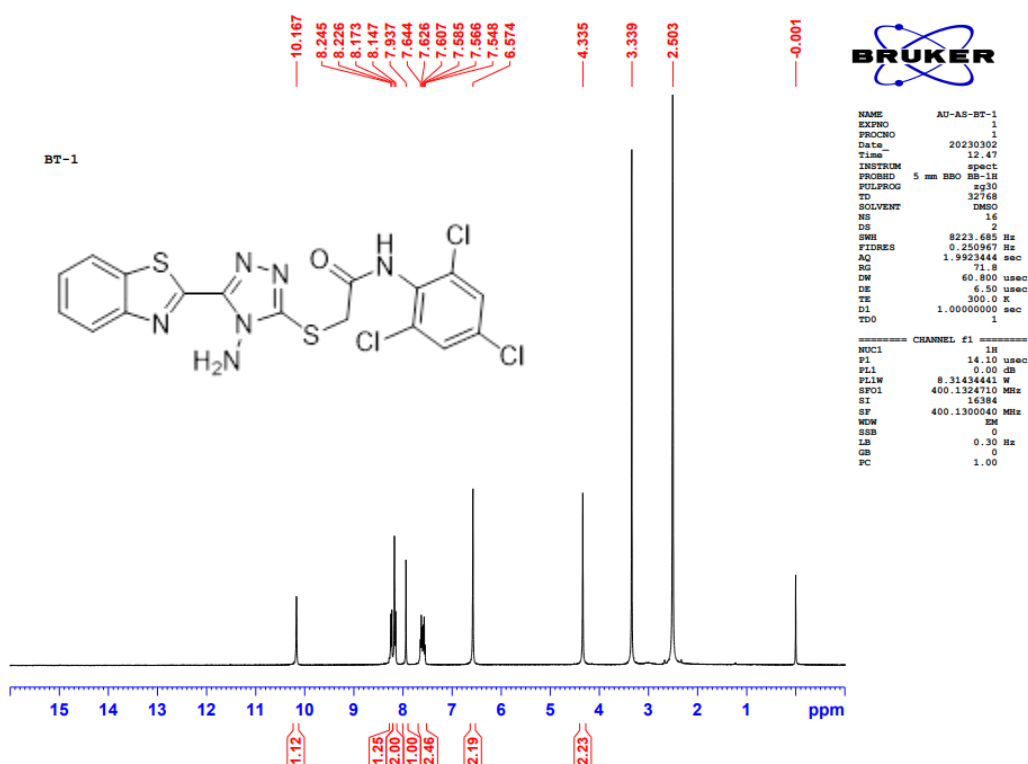


Figure 13: Representative <sup>1</sup>H NMR spectrum of compound 8a

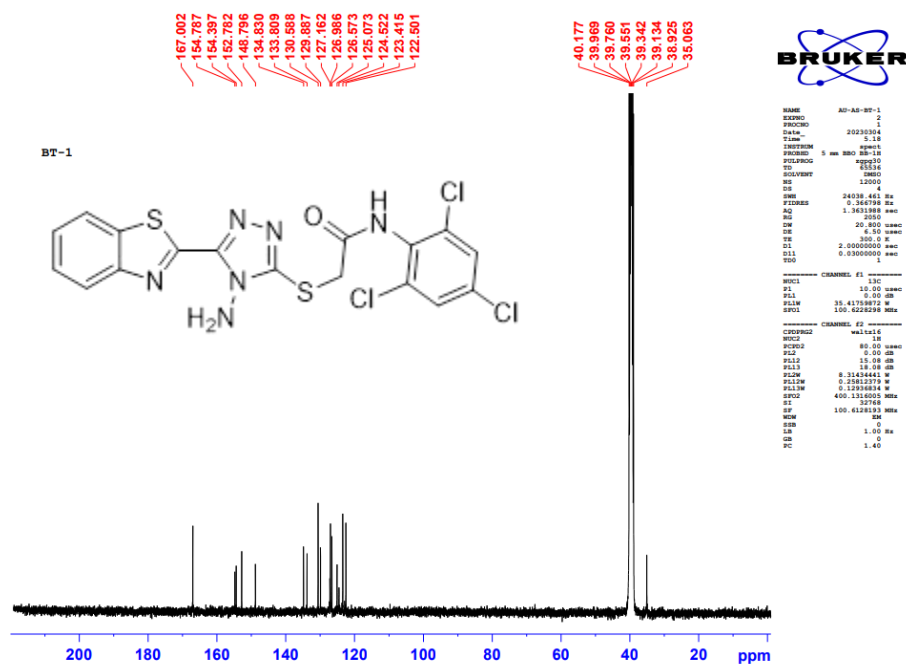


Figure 14: Representative <sup>13</sup>C NMR spectrum of compound 8a

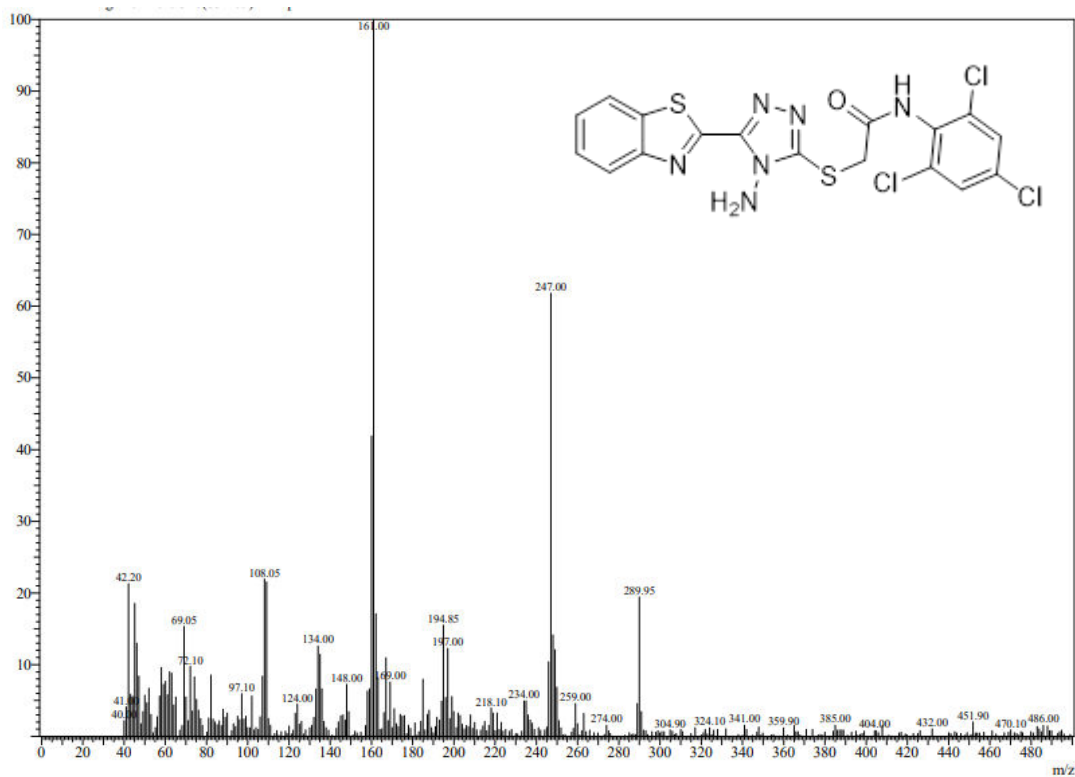


Figure 15: Representative mass spectrum of compound 8a

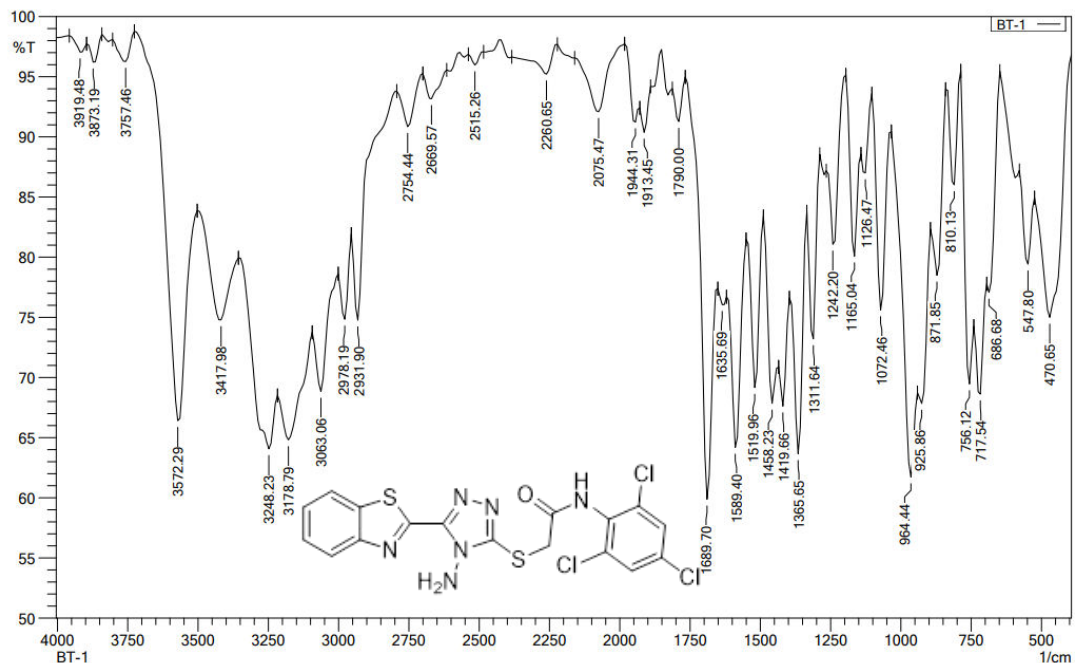


Figure 16: Representative FT-IR spectrum of compound 8a

➤ Spectral data of compound 8b

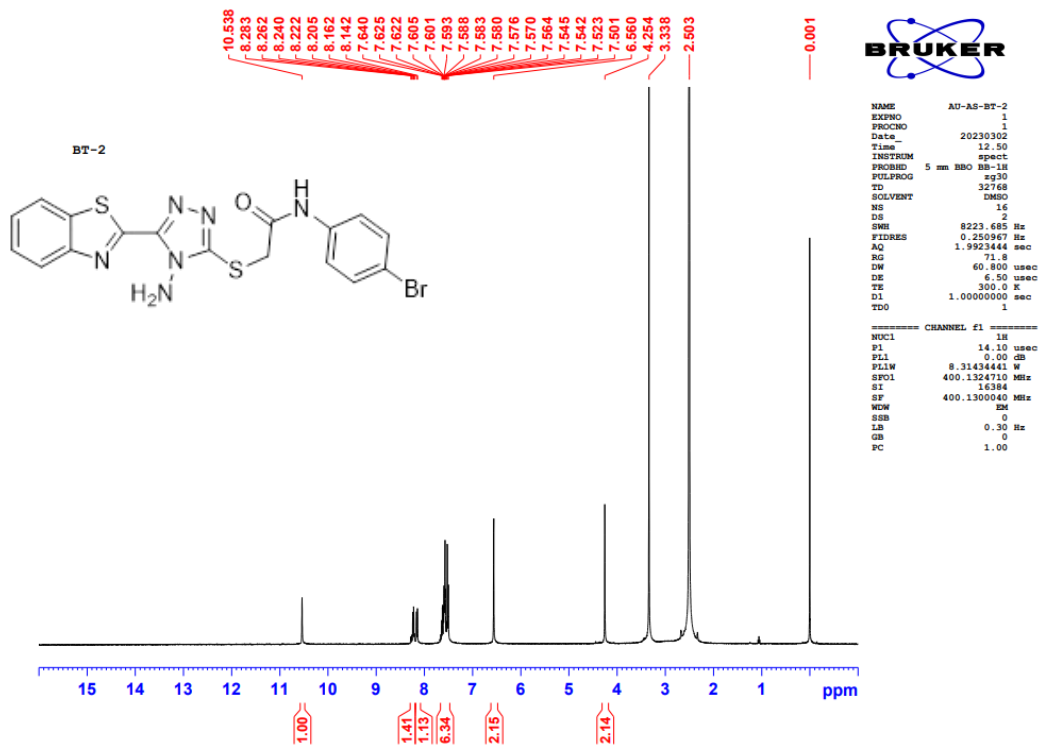


Figure 17: Representative <sup>1</sup>H NMR spectrum of compound 8b

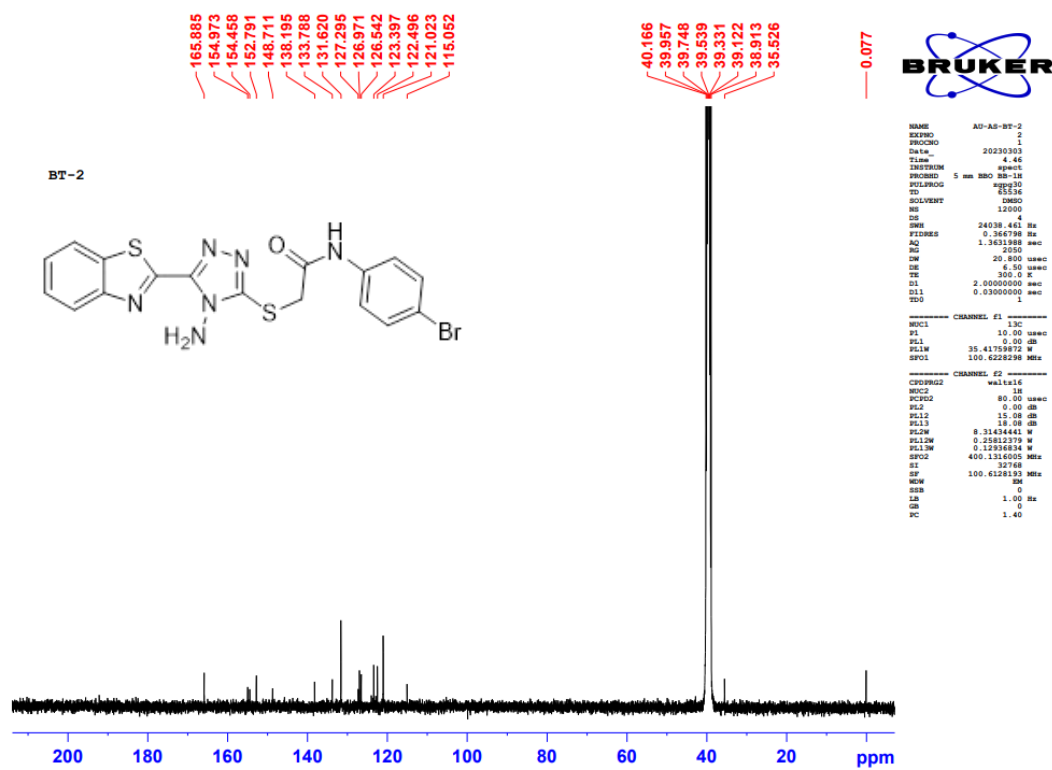


Figure 18: Representative  $^{13}\text{C}$  NMR spectrum of compound 8b

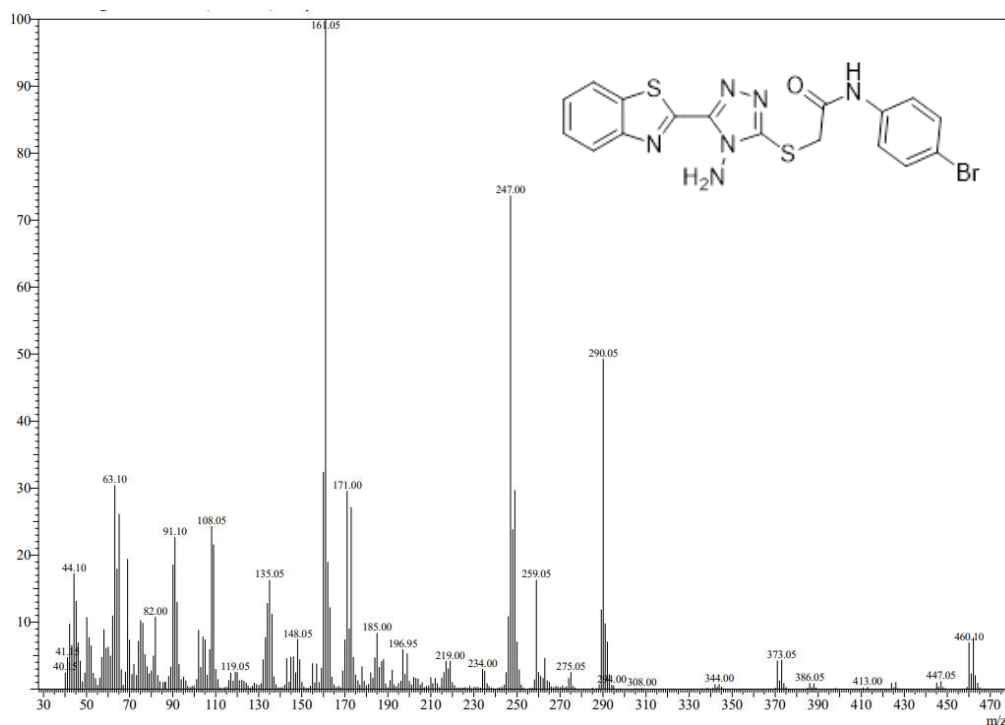


Figure 19: Representative mass spectrum of compound 8b



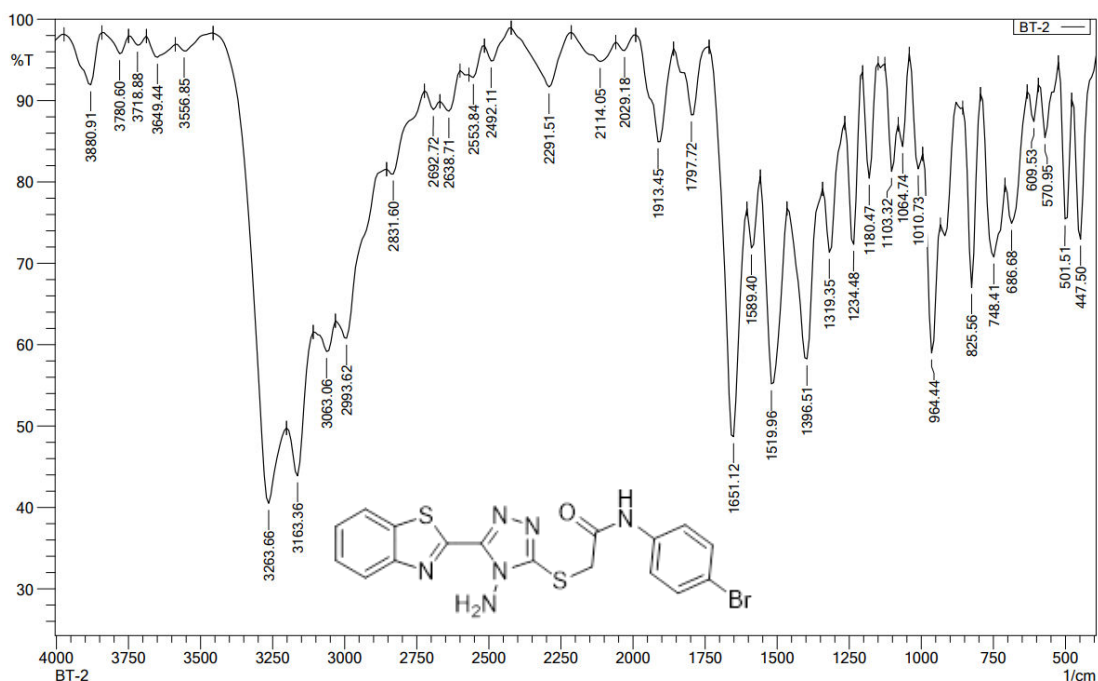


Figure 20: Representative FT-IR spectrum of compound 8b

➤ Spectral data of compound 8c

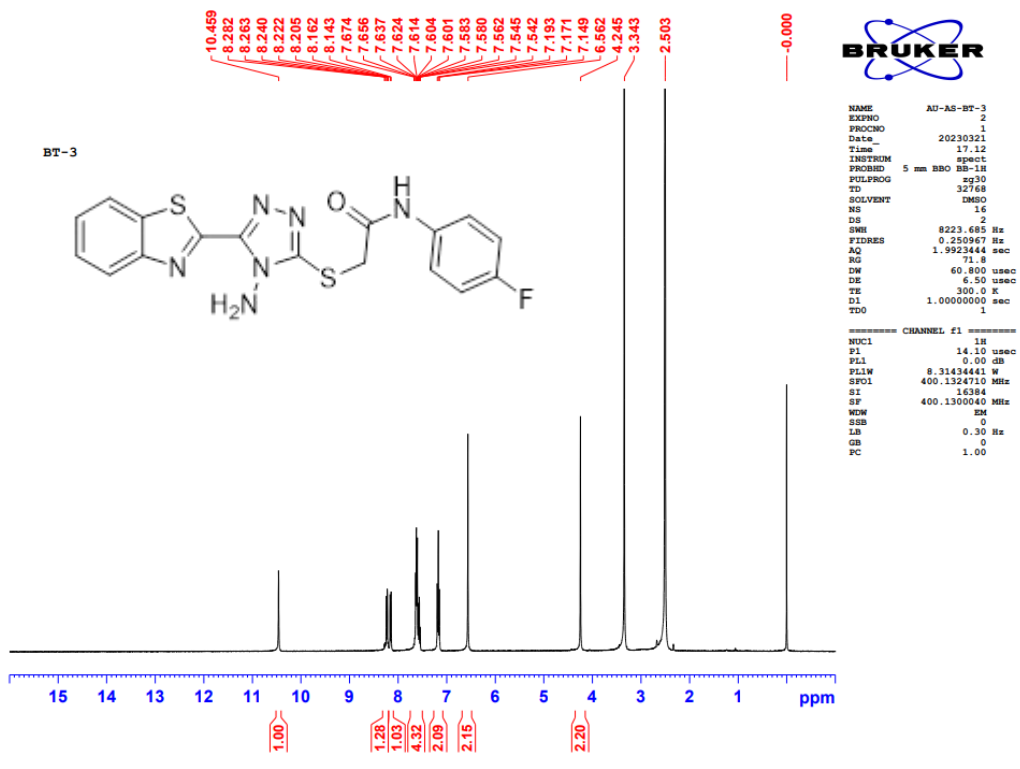


Figure 21: Representative <sup>1</sup>H NMR spectrum of compound 8c

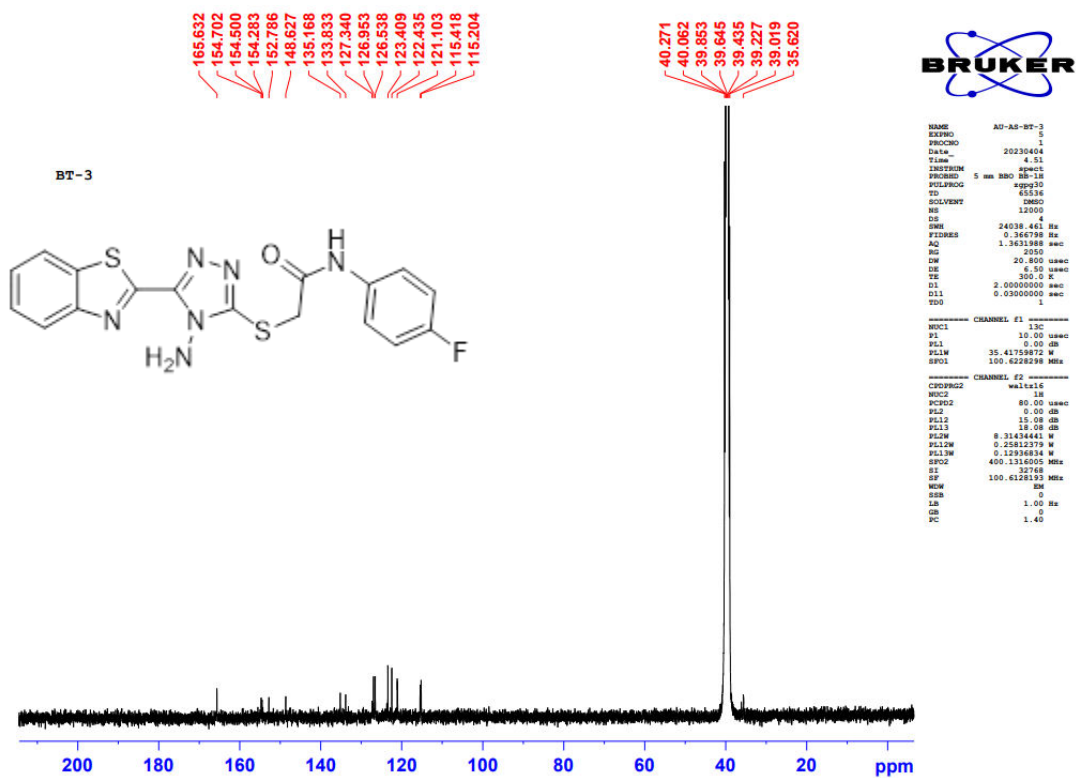


Figure 22: Representative <sup>13</sup>C NMR spectrum of compound 8c

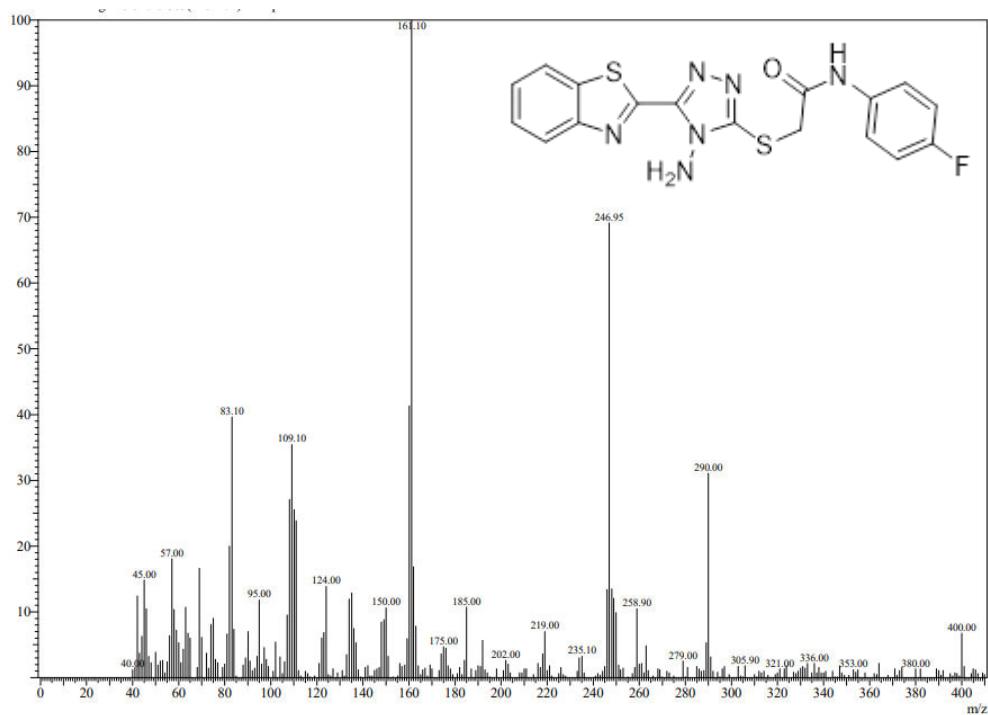


Figure 23: Representative mass spectrum of compound 8c

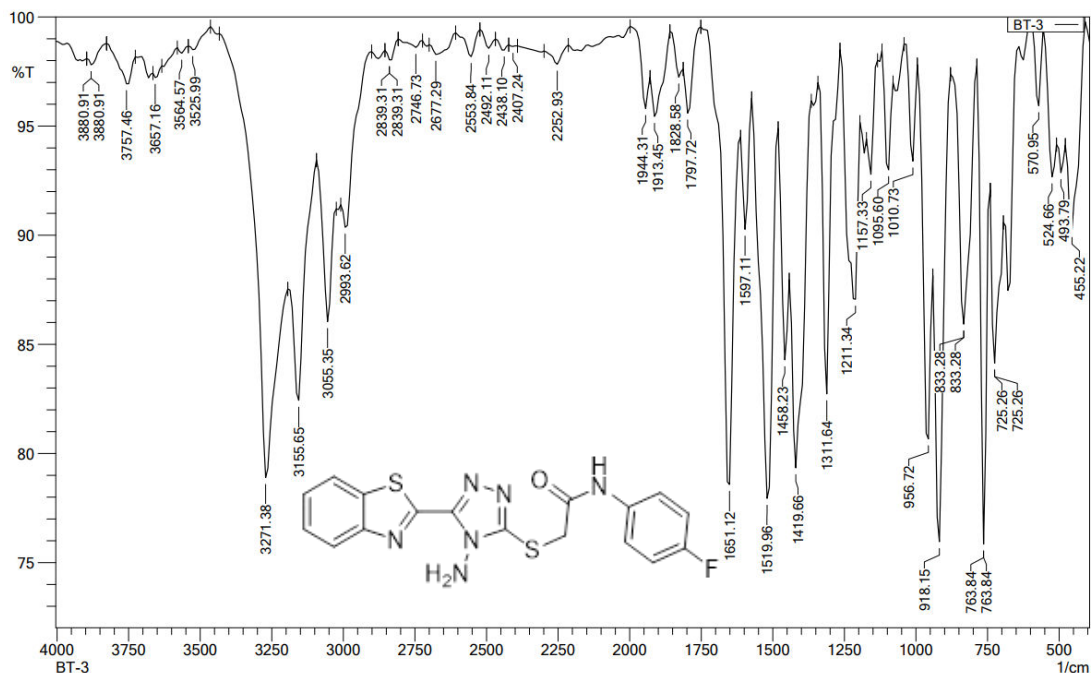


Figure 24: Representative FT-IR spectrum of compound 8c

➤ Spectral data of compound 8d

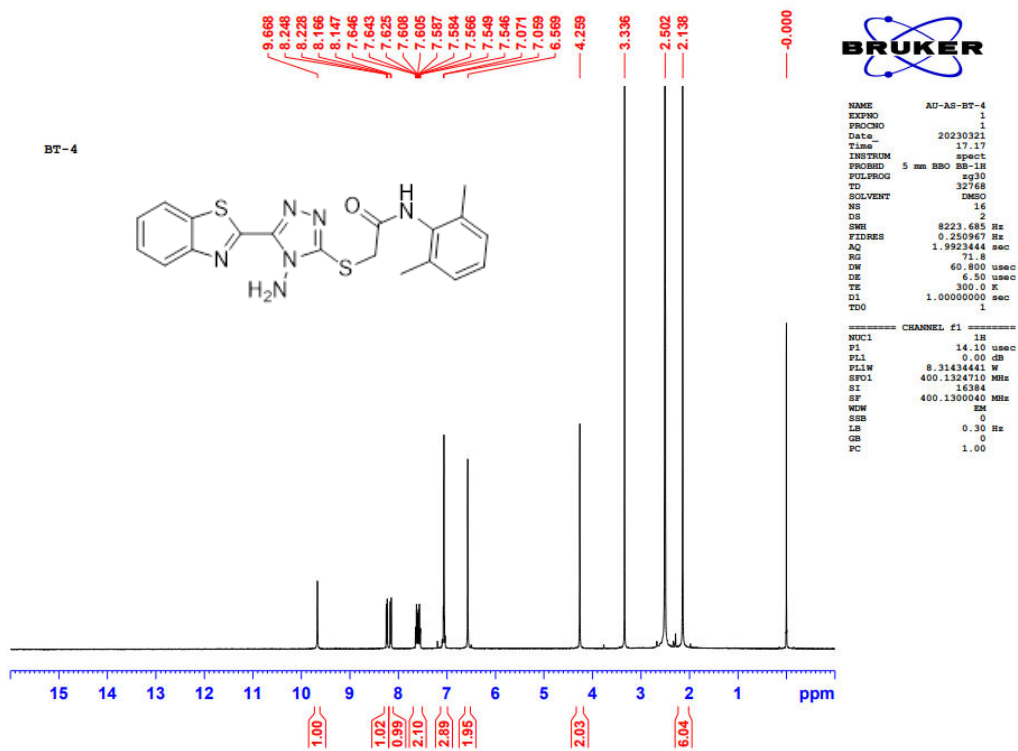


Figure 25: Representative  $^1\text{H}$  NMR spectrum of compound 8d

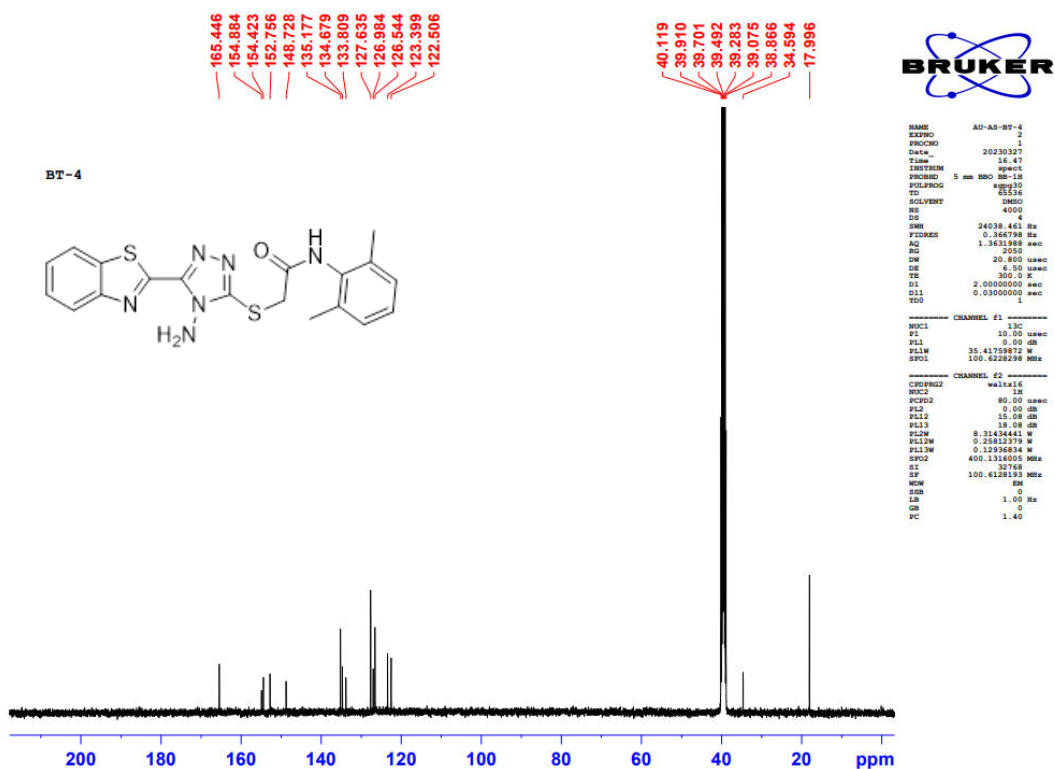


Figure 26: Representative <sup>13</sup>C NMR spectrum of compound 8d

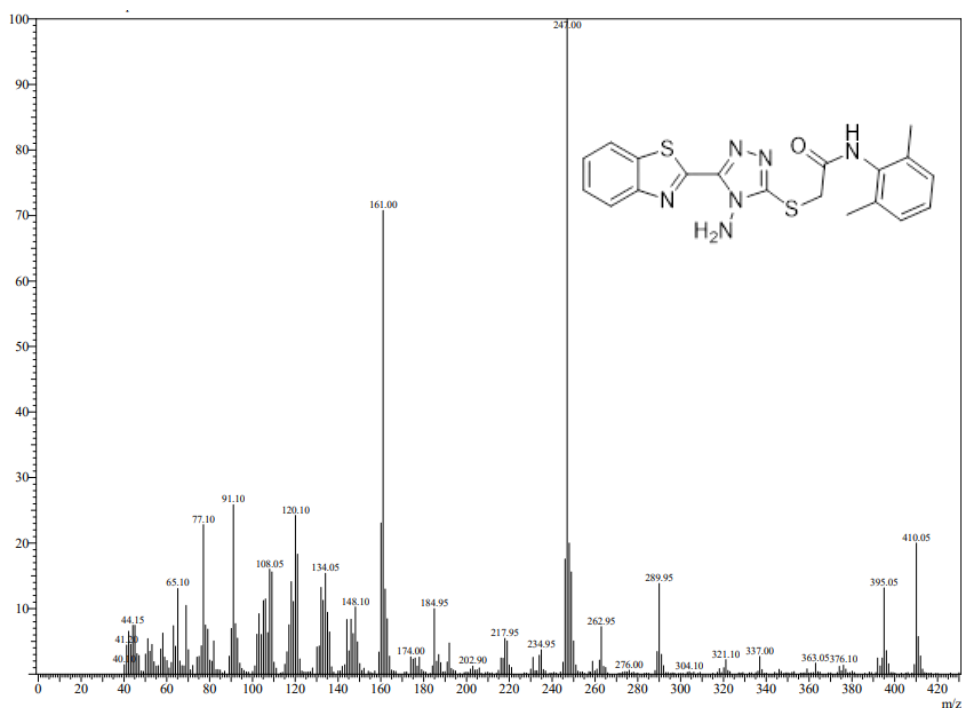


Figure 27: Representative mass spectrum of compound 8d

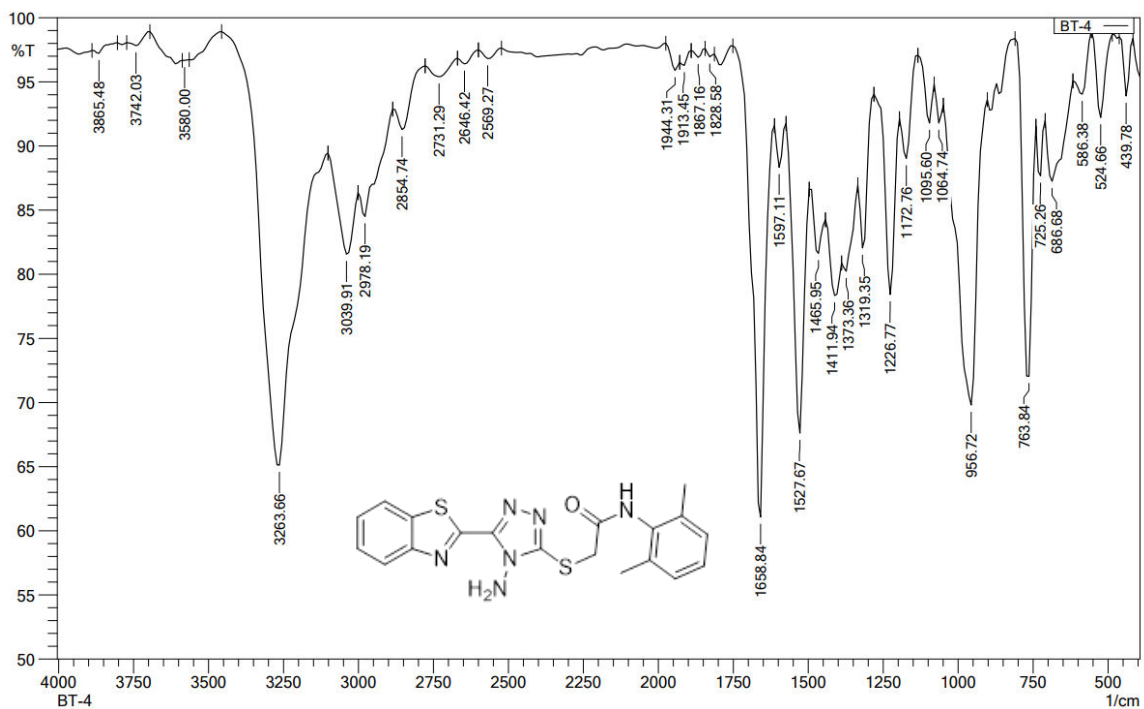


Figure 28: Representative FT-IR spectrum of compound 8d

➤ Spectral data of compound 8e

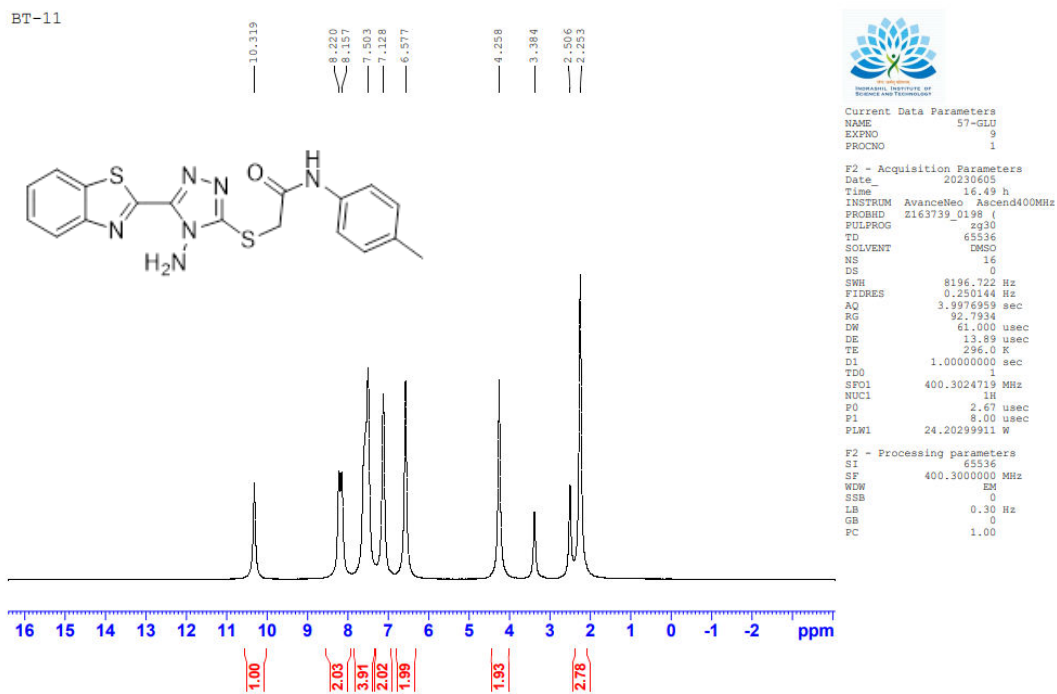


Figure 29: Representative <sup>1</sup>H NMR spectrum of compound 8e

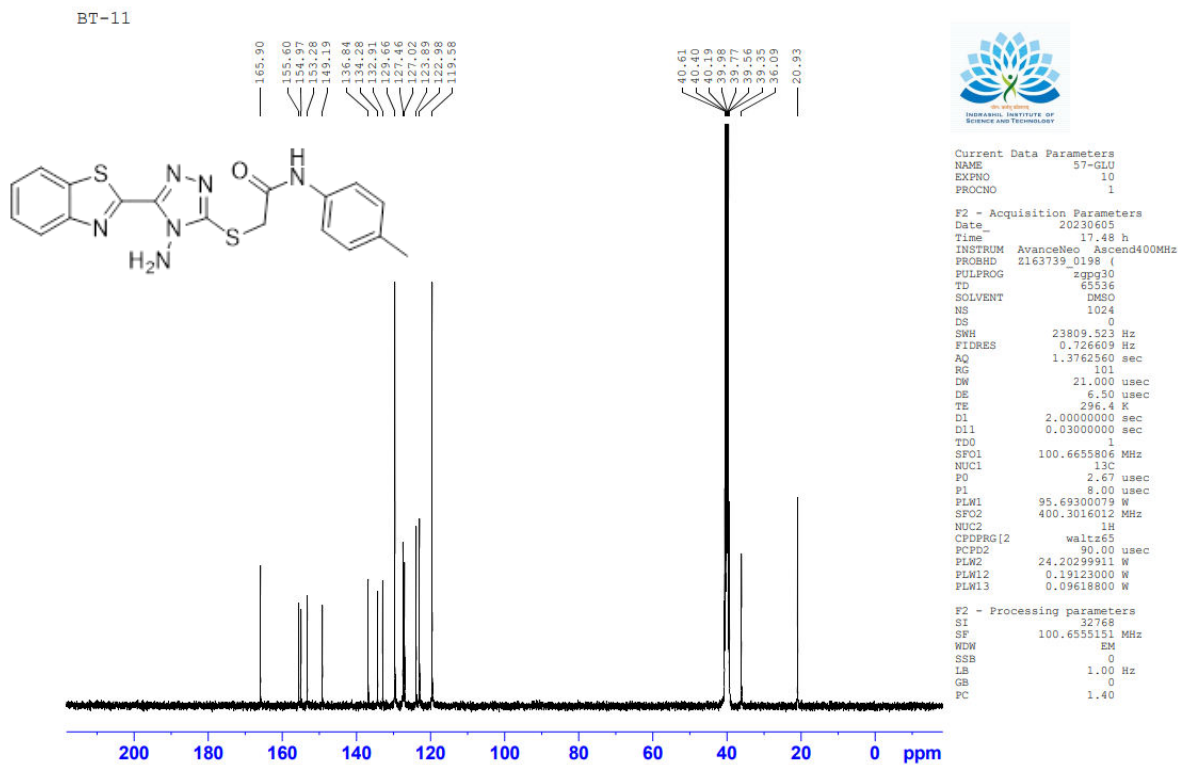
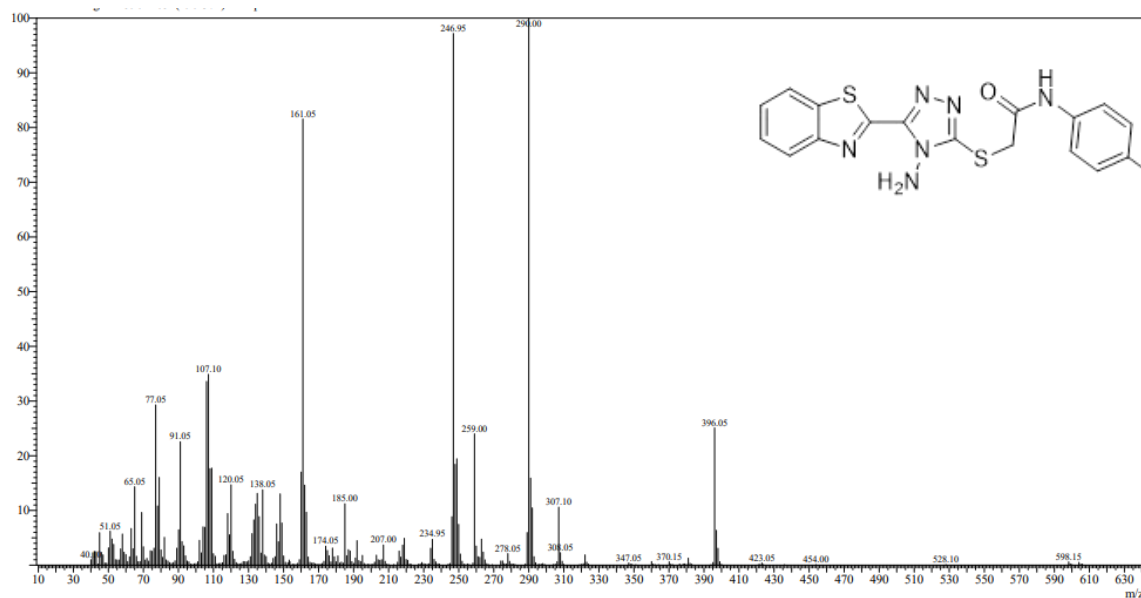


Figure 30: Representative  $^{13}\text{C}$  NMR spectrum of compound 8e



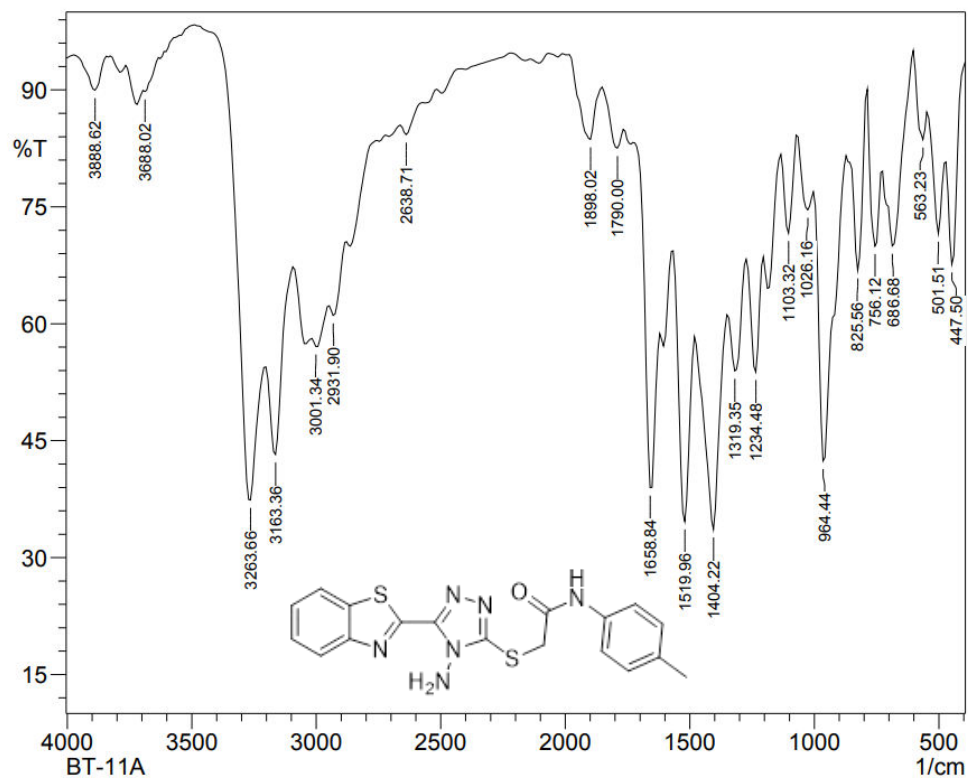


Figure 32: Representative FT-IR spectrum of compound 8e

➤ Spectral data of compound 8f

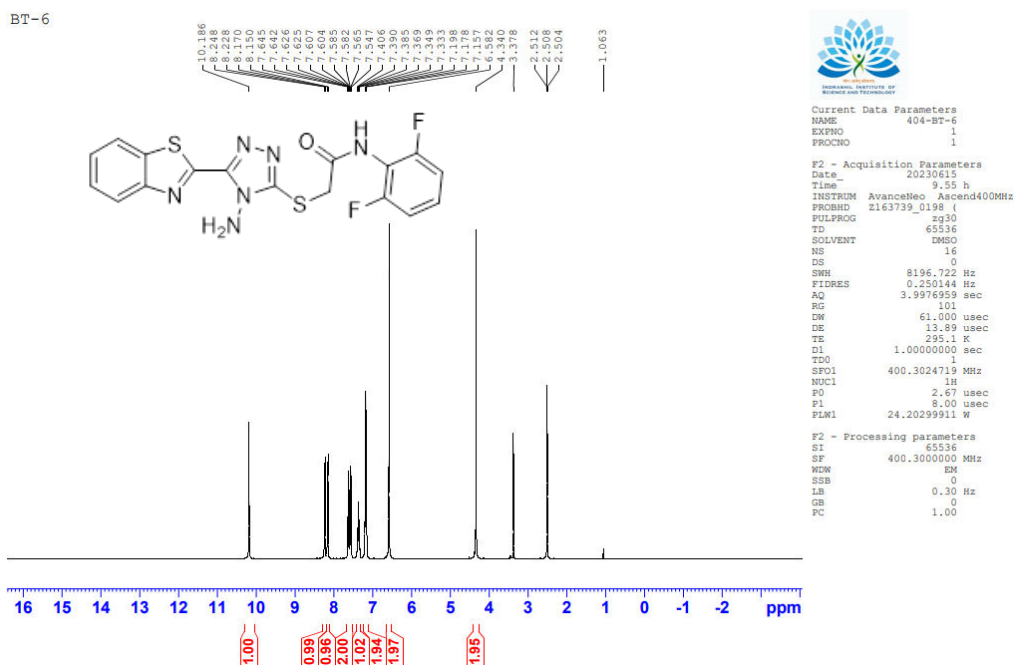


Figure 33: Representative <sup>1</sup>H NMR spectrum of compound 8f



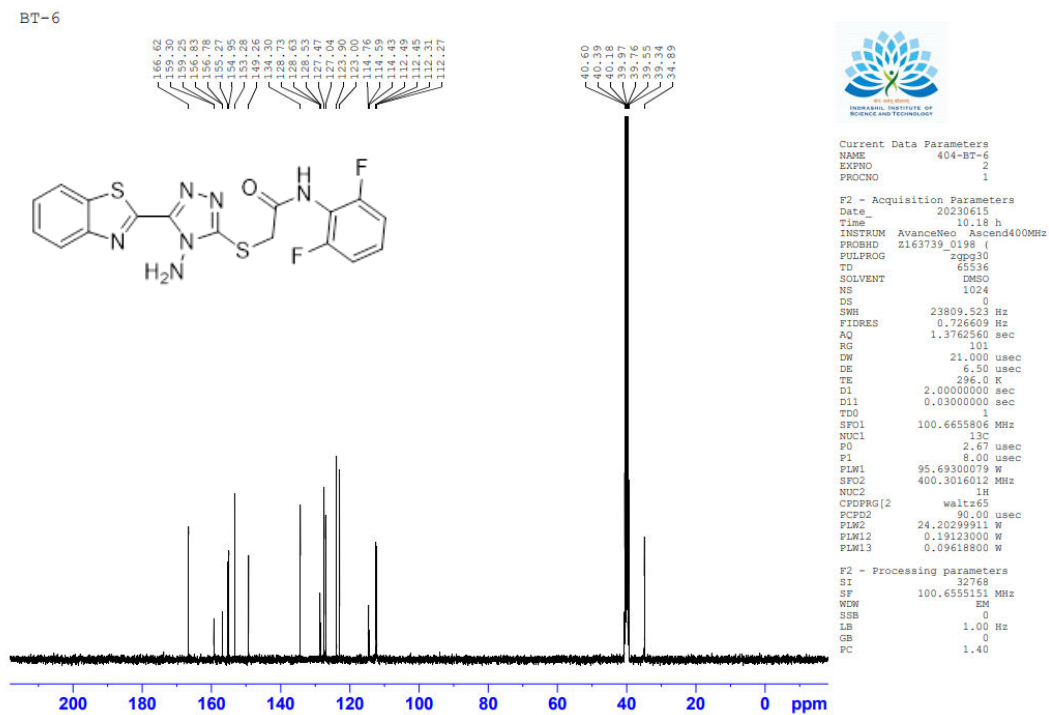


Figure 34: Representative  $^{13}\text{C}$  NMR spectrum of compound 8f

➤ Spectral data of compound 8g

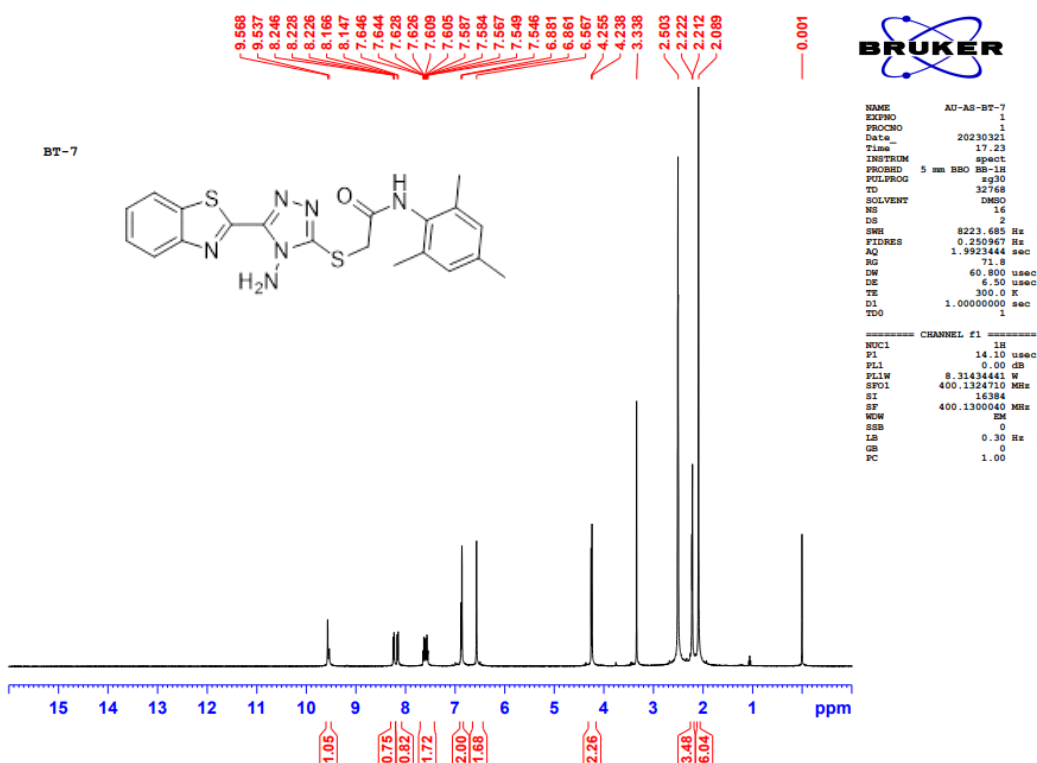


Figure 35: Representative  $^1\text{H}$  NMR spectrum of compound 8g



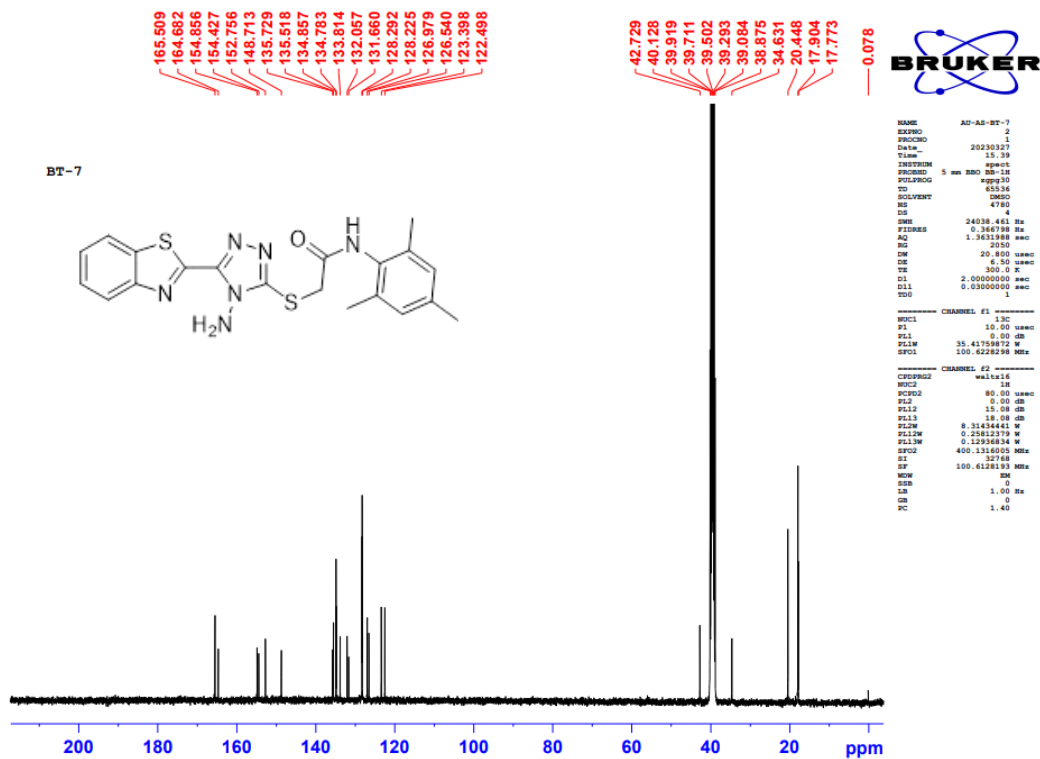


Figure 36: Representative  $^{13}\text{C}$  NMR spectrum of compound 8g

➤ Spectral data of compound 8h

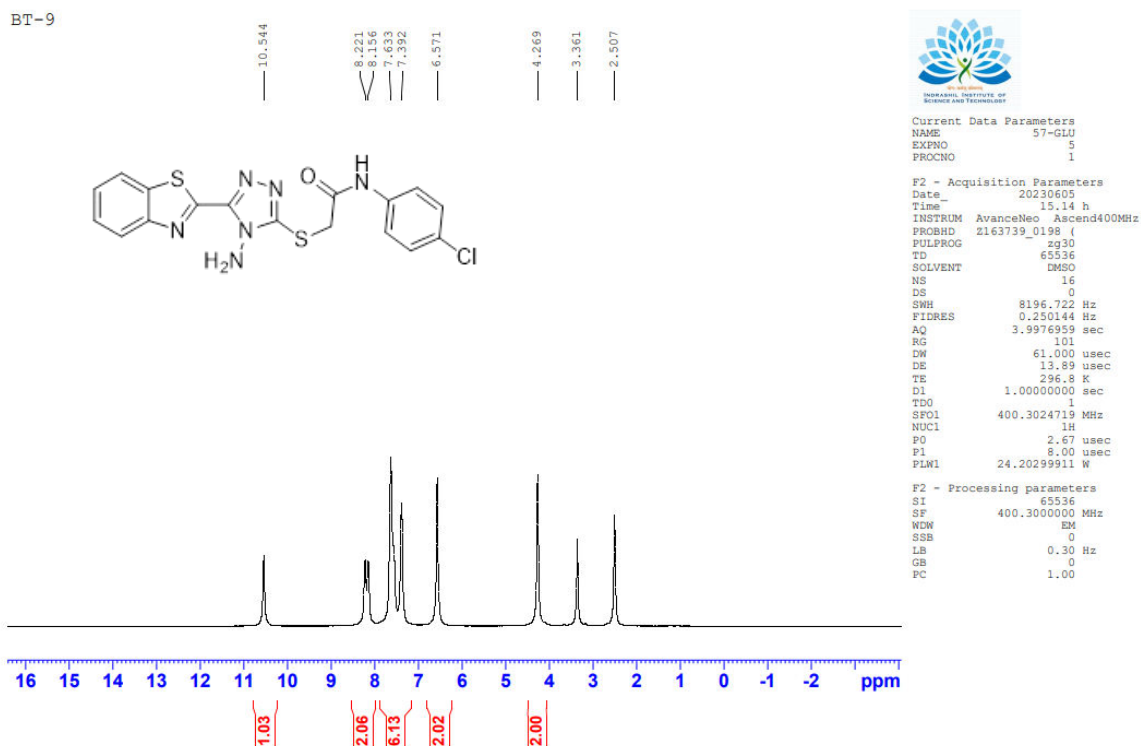


Figure 37: Representative  $^1\text{H}$  NMR spectrum of compound 8h

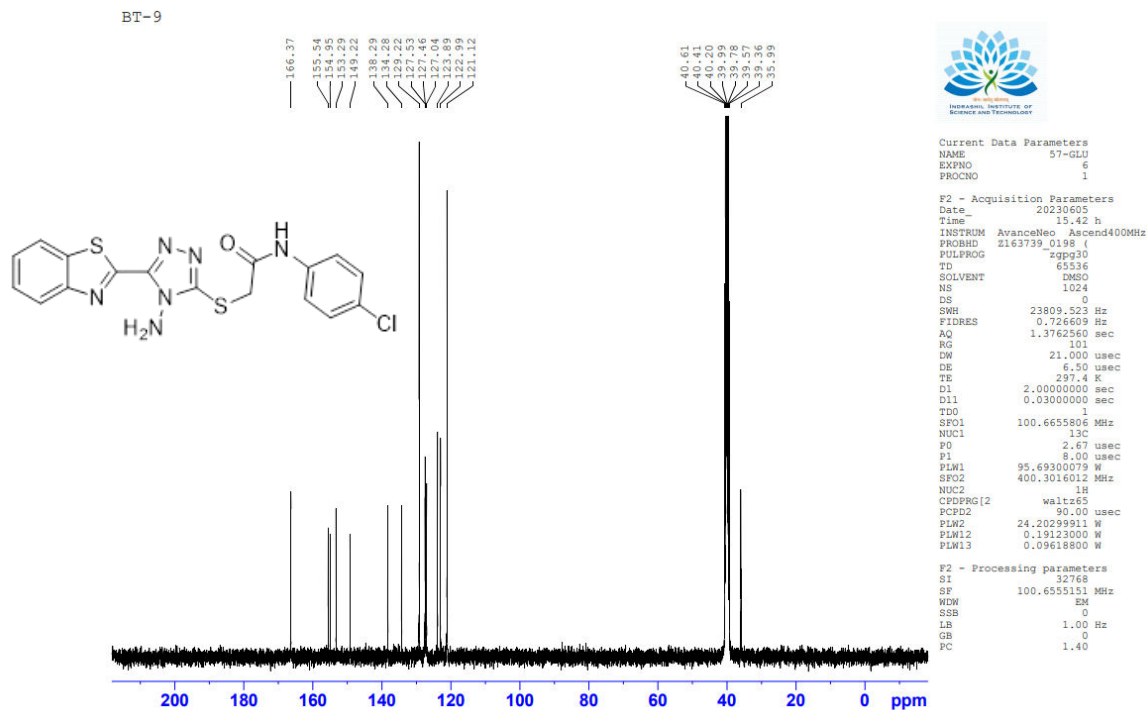


Figure 38: Representative  $^{13}\text{C}$  NMR spectrum of compound 8h

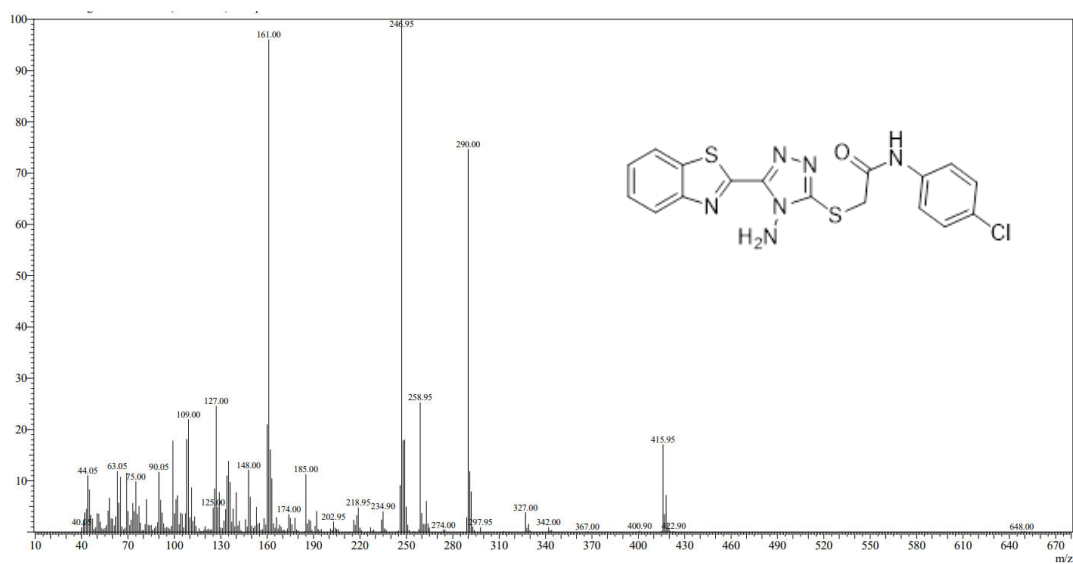


Figure 39: Representative mass spectrum of compound 8h

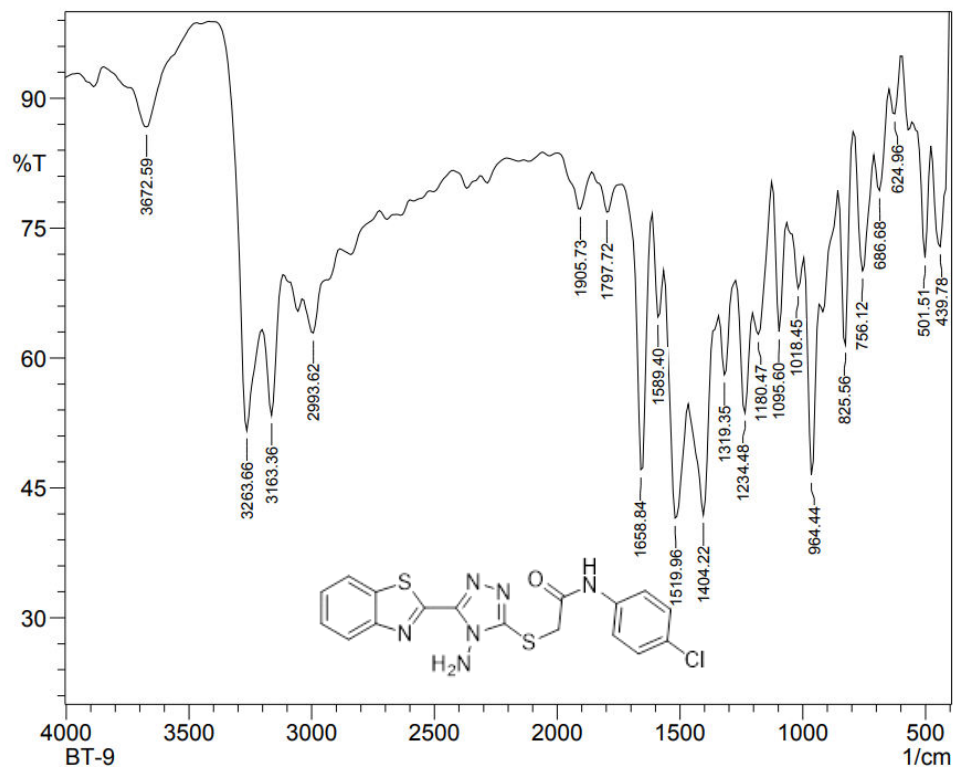


Figure 40: Representative FT-IR spectrum of compound 8h

➤ Spectral data of compound 8i

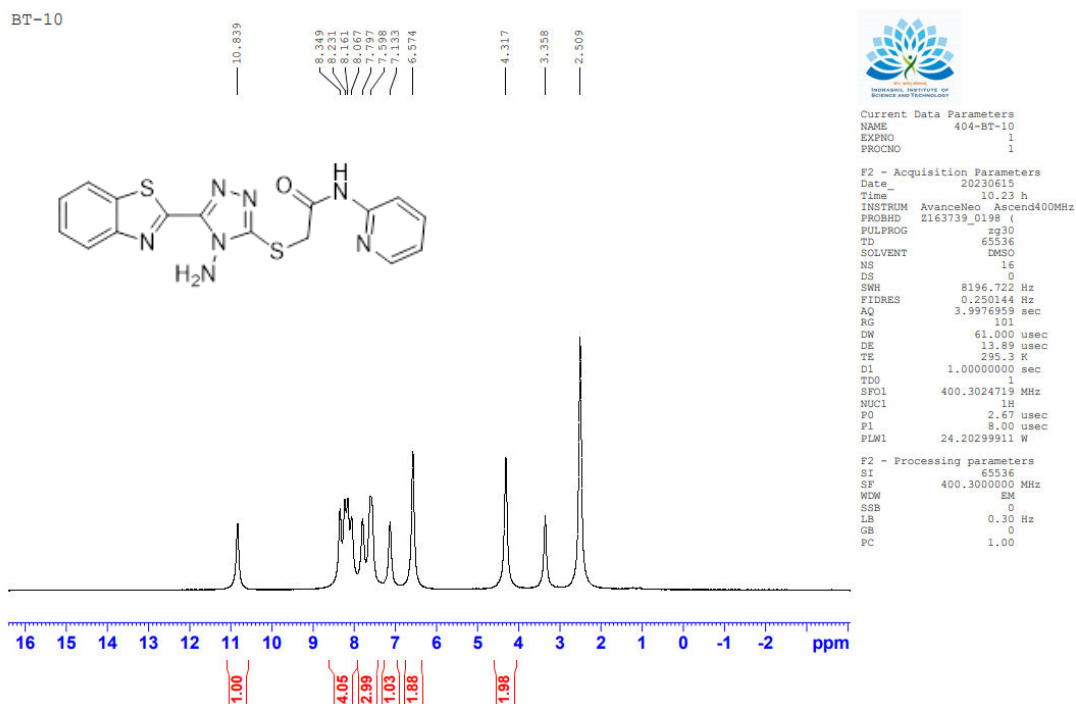


Figure 41: Representative <sup>1</sup>H NMR spectrum of compound 8i

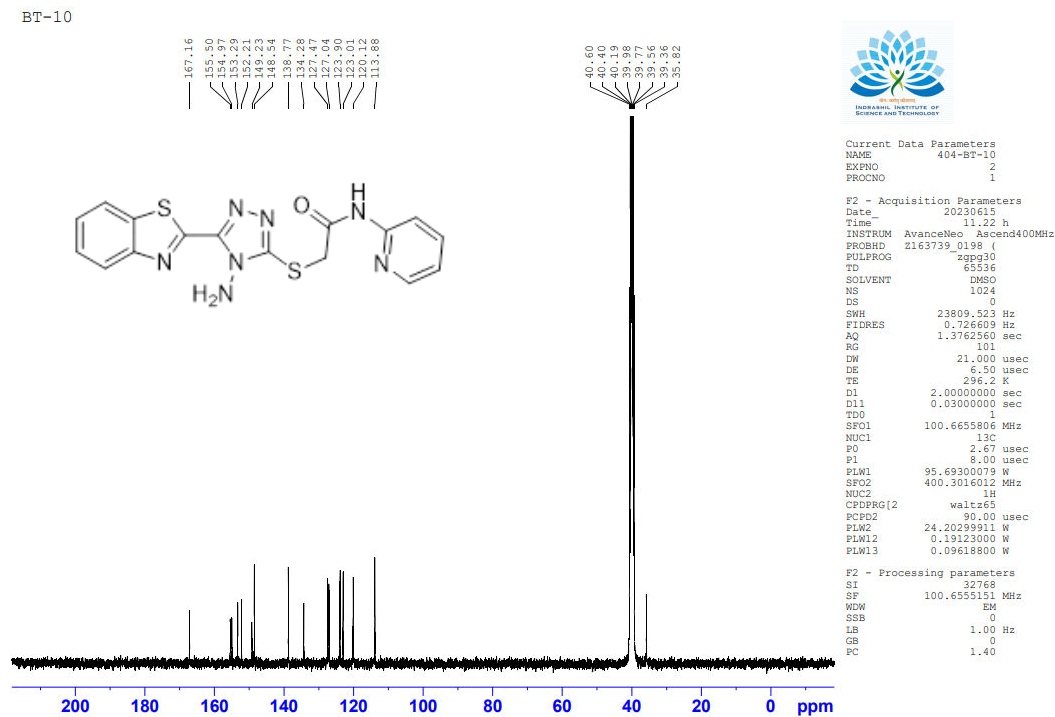


Figure 42: Representative <sup>13</sup>C NMR spectrum of compound 8i

➤ Spectral data of compound 8j

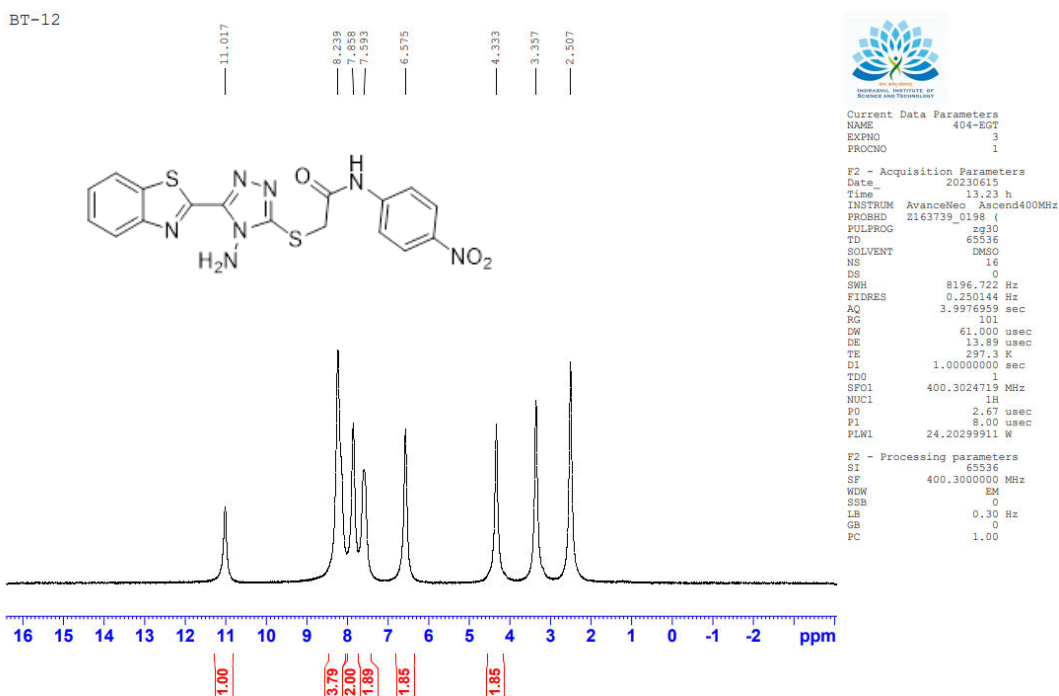


Figure 43: Representative <sup>1</sup>H NMR spectrum of compound 8j

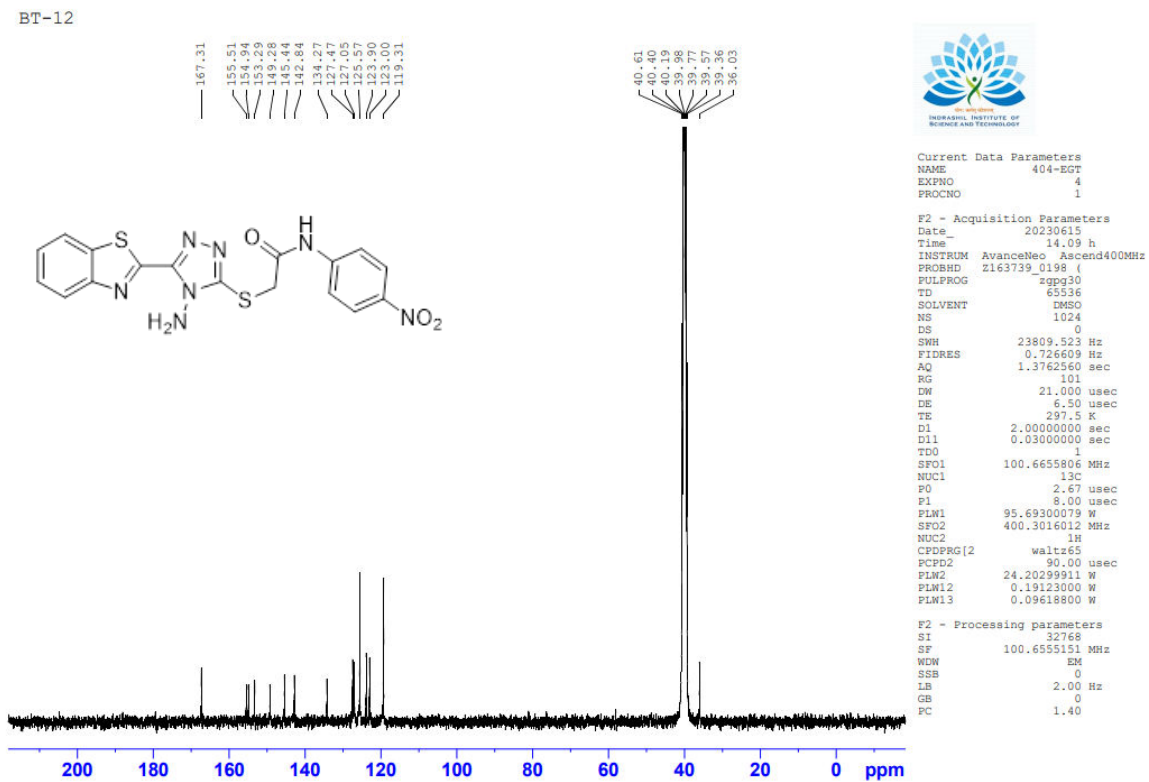


Figure 44: Representative <sup>13</sup>C NMR spectrum of compound 8j